Stony Brook University

DATA ACQUISITION SYSTEM FOR METEOR AND COSMIC RAY DETECTION

A Thesis Presented
by

Subodh Chiwate

to
The Graduate School
in Partial Fulfillment of the
Requirements
for the Degree of

Master of Science
in
Electrical Engineering
Stony Brook University

December 2009

Stony Brook University
The Graduate School

Subodh Chiwate

We, the thesis committee for the above candidate for the
Master of Science degree,
hereby recommend acceptance of this thesis.

Mónica F. Bugallo, Thesis Advisor
Assistant Professor, Department of Electrical & Computer Engineering

Petar M. Djurić, Second Reader
Professor, Department of Electrical & Computer Engineering

This thesis is accepted by the Graduate School

Lawrence Martin
Dean of the Graduate School

Abstract of the Thesis

DATA ACQUISITION SYSTEM FOR METEOR AND COSMIC RAY DETECTION

by

Subodh Chiwate

Master of Science

in

Electrical Engineering

Stony Brook University

2009

The enigma regarding the source of cosmic rays has bewildered cosmologists and astrophysicists since the discovery of ultra high energy cosmic rays (UHECR). Identifying the location of their source will give us a highly valuable insight about the origins and evolution of the Universe. Many different methods for cosmic ray detection have been developed and are still being used for the purpose. In this thesis, a comparatively new radar-based approach for cosmic ray detection is explored.

The work proposes a data acquisition system (DAQ) which may be able to detect cosmic rays and correlate the results with existing conventional detector arrays. The conventional back scatter radar approach used by military and weather applications proves to be less effective hence the alternative forward scatter technique is proposed. Although all the modules of the system have been explored individually in different fields of science,

the real innovation of this work lies in integrating these modules. The work provides a brief overview of the components and provides the criterion considered while selecting them. The ideas proposed in this work are in nascent stage of implementation and hence provide an excellent opportunity to identify the areas of concern before full scale implementation. Results included in the work provide a credible evidence of the concept proposed.

The thesis is organized in the way the problem was unfurled. It is divided into five chapters, the first four addressing four different issues and the fifth containing conclusion and proposed future work. The first four chapters are dedicated to the brief history and basic physics involved, the system overview, software defined radio GNU Radio and signal processing, respectively. Each chapter provides the currently implemented system features, challenges discovered during the work and possible solutions to the open questions relevant to this work.

The motivation behind proposing this DAQ is to exploit its great advantages of being compact, cost efficient, portable and reconfigurable. The easy availability of the components and simple installation are extremely desirable features considering the large area of detection. The ultimate goal is to propose a low cost DAQ system and detection algorithm that are capable of detecting cosmic rays in a computationally optimal and reliable way.

To all my mentors, for believing in my abilities,
my friends, for accompanying me through the journey,
and my family for all their affection.

Contents

List of Figures

Acknowledgments

"Real knowledge is to know the extent of one's ignorance."
Confucius (551 BC - 479 BC)

I would like to express my deepest gratitude to my advisors, Professor Mónica F. Bugallo and Professor Petar M. Djurić. I thank them for their motivation, encouragement and guidance without which, this work would not have been possible.

I would like to thank Professor Mónica F. Bugallo for giving me an opportunity to teach and be part of educational workshops. With these opportunities I was able to regain my curiosity, which probably got buried under the massive volume of expectations over the years. I would specially like to thank Professor Petar M. Djurić for giving me the opportunity to work with him, even when all conventional statistics suggested otherwise. His patience with all my extremely infeasible ideas and encouragement to analyze failures have definitely made me a better student for the rest of my life.

I would like to thank all current and previous members of COSINE lab, Bingxin Shen, Kevin Mernick, Zejie Zhang, Mingyi Hong, Ting Lu, Yao Li, Cagla Tasdemir, Pingyi Xiong, Vibha Mane, Shishir Dash, Jin Xu. I would specially like to thank Pau Closas from University of Barcelona, who visited us during the summer of 2008. The long lunch time discussions with him were pleasant experience, but more importantly he shared his research experience and encouraged me to tackle situations in a more professional manner.

I am extremely grateful to Professor Michael Marx and Professor Helio Takai for giving me an opportunity to work on the MARIACHI project. I had a really great time during the summer workshops. I would like to thank Dima Vavilov, John Hover, Dr. Gillian Winters, Richard Lefferts and other members of MARIACHI group for their co-operation and support during the project.

I am grateful to all my friends for always making work a pleasant experience for me. They always helped me by providing rejuvenating distractions. My stay at Stony Brook was a great learning experience both personally and professionally.

I would finally like to thank everyone who has believed in my abilities and more importantly those who have challenged them. Although the results of this work are not going to change the world but the experience was enlightening enough to make me believe that may be one day I can.

Chapter 1

Introduction

Intriguing mysteries of the Universe have kept mankind mystified since the beginning of civilization. High-energy cosmic rays are just such a mystery. Cosmic rays have been studied extensively and progressively, leading to revelation of many answers to questions about the Universe.

1.1 What are cosmic rays?

Cosmic rays are nuclei and elementary particles travelling at very high speeds across the Universe. Millions of such high energy particles interact with the Earth's atmosphere on daily basis. Those which have large kinetic energies interact with nuclei of air atoms, thus initiating cascades of secondary particles, which are also known as extensive air showers (EASs) [15]. The Oh-My-God particle is the nickname given to a particle observed in 1991 in Utah [2] and estimated to have an energy of approximately 3×10^{20} electron volts - in other words, it was a subatomic particle with energy equal to that of a baseball (140 g) moving at about 27 m/s (60mph) [16]. In general the energies of subatomic particles that comprise ultra high energy cosmic rays (UHECR) are between 10^{18} and 10^{20} eV.

1.1.1 Scales of energy

Scientists measure the energies of fast-moving particles like those in cosmic rays and particle accelerators in units called electron volts, abbreviated eV. An electron volt is the amount of energy that one electron gains when it is

accelerated by an electrical potential of one volt. (A flashlight battery has about 1.5 volts.) Electrons in a television set are accelerated by the picture tube to an energy of about 50,000 eV. When they strike the screen, they make it glow [1].

The most powerful man-made particle accelerator, Large Hadron Collider (LHC), can accelerate protons to nearly 7 TeV [17]. The highest-energy cosmic ray particle ever observed had an energy 40 million times higher than the protons at the LHC.

Energy	**Shorthand Designation**
10^3 eV	1 keV (kilo)
10^6 eV	1 MeV (mega)
10^9 eV	1 GeV (giga)
10^{12} eV	1 TeV (tera)
10^{15} eV	1 PeV (peta)
10^{18} eV	1 EeV (exa)
10^{21} eV	1 ZeV (zetta)

Table 1.1: Energy values and shorthand notations

1.1.2 A timeline of high-energy cosmic rays study [1]

- **1912:** In a balloon at an altitude of 5000 meters, Victor Hess, the father of cosmic ray research, discovered 'penetrating radiation' coming from space. His was the first of many adventurous journeys made by physicists to study cosmic rays.

- **1927:** Using a cloud chamber, Dimitry Skobelzyn photographed the first ghostly tracks left by cosmic rays.

- **1932:** While watching the tracks of cosmic ray particles passing through his cloud chamber, Carl Anderson discovered antimatter in the form of the anti electron, later called the positron. A positron is a particle exactly like an electron, but with an opposite, positive charge. A debate raged over the nature of cosmic rays. According to a theory of Robert Millikan, they were gamma rays from space – hence the name 'cosmic rays'. But evidence was mounting that cosmic rays were, in fact, mostly energetic particles.

- **1937:** Seth Neddermeyer and Carl Anderson discovered the elementary subatomic particle called the muon in cosmic rays. The positron and the muon were the first of a series of subatomic particles discovered using cosmic rays – discoveries that gave birth to the science of elementary particle physics. Particle physicists used cosmic rays for their research until the advent of particle accelerators in the 1950s.

- **1938:** Pierre Auger, who had positioned particle detectors high in the Alps, noticed that two detectors located many meters apart both signaled the arrival of particles at exactly the same time. Auger had discovered showers of secondary subatomic particles caused by the collision of primary high-energy particles with air molecules. On the basis of his measurements, Auger concluded that he had observed showers with energies of 10^{15} eV – ten million times higher than any known before.

- **1946:** Groups led by Bruno Rossi in the USA and Georgi Zatsepin in Russia started experiments on the structure of Auger showers. These researchers constructed the first arrays of correlated detectors to detect air showers.

- **1949:** Enrico Fermi put forth an explanation for the acceleration of cosmic rays. In Fermi's cosmic ray 'shock' accelerator, protons speed up by bouncing off moving magnetic clouds in space. Exploding stars (supernovae) are believed to act as such cosmic accelerators, but they alone cannot account for the highest-energy cosmic rays.

- **1962:** John Linsley and collaborators discovered the first cosmic ray with an energy of about 10^{20} eV in the Volcano Ranch array in New Mexico, USA.

- **1966:** In the early 1960s, Arno Penzias and Robert Wilson discovered that low-energy microwaves permeate the Universe. Kenneth Greisen,Vadem Kuzmin and Georgi Zatsepin (GZK) pointed out that high-energy cosmic rays would interact with the microwave background. The interaction would reduce their energy, so that particles traveling long intergalactic distances could not have energies greater than 5×10^{19} eV.

- **1967:** An array of over 200 water-Cherenkov detectors covering 12 km^2 was operated for over 20 years from 1967 at Haverah Park in England. Although designed before the GZK prediction, the data have contributed in a major way to our understanding of cosmic rays at the highest energies. For the Auger Observatory, the demonstration that water could be kept bacteria-free in a sealed container for over 25 years was of major importance as were early studies of inclined showers and of the time structure of the shower front. A tank was opened at the 'end of project' party on July 31 1987. The water had been in the tank for 25 years but was quite drinkable!

- **1991:** The Fly's Eye cosmic ray research group in the USA observed a cosmic ray event with an energy of 3×10^{20} eV. Events with energies of 10^{20} eV had been reported in the previous 30 years, but this was clearly the most energetic.

- **1994:** The Akeno Giant Air Shower Array (AGASA) Group in Japan and the Yakutsk group in Russia reported events with energies of 2×10^{20} eV. The Fly's Eye event and these other events are higher in energy than any seen before. None of them seemed to point back to an astrophysical object that could impart such enormous energies.

1.1.3 Cosmic ray detection

The technology of recording cosmic ray showers has improved over the years. At first, they were studied using instruments such as ionization chambers, Geiger counters, and cloud chambers. These instruments recorded a signal when an energetic charged particle passed through them. In the late 1920s, the French scientist Pierre Auger discovered the phenomenon of extensive air showers using these techniques. What he found was that very energetic cosmic rays were capable of producing showers of secondary particles which spread over a large area up to hundreds of meters. These methods only detect particles that reach the ground, but do not tell us about how a cosmic ray shower develops in the atmosphere.

A new technique was developed in the 1980s based on the phenomenon of atmospheric fluorescence. When a charged particle passes close to molecules in the atmosphere, it transfers some energy to the molecules, in effect 'shaking up' the electrons inside. The molecules respond by emitting light as their

electrons return to their normal arrangement, and this light is known as fluorescence. Nitrogen molecules, which make up most of the air, make blue fluorescent light. This light can be detected by a sensitive instrument called photomultiplier. Even so, the light is so faint that it can only be observed on moonless nights without clouds. This technique has been successfully used by the Fly's Eye experiment in Utah [2], and is also being used by experiments including HiRes and the Pierre Auger Observatory [1].

Another technique, useful for measuring cosmic rays that reach the ground, uses a phenomenon called the Cerenkov effect. In transparent materials, the speed of light is less than its value in vacuum (3×10^5 km/s). In water, for example, light travels at 70 percent of its speed in vacuum. When a high energy charged particle, such as a cosmic ray, passes through the water at speeds greater than the speed of light in the medium, it creates a shock front of light that spreads out in a cone around the particle. Photomultiplier tubes placed in the water detect the Cerenkov light [3]. An array of these detectors was used in an experiment in Haverah Park, England, for more than 20 years until 1991. Tanks of water using photomultipliers to see Cerenkov light are also being used by the Pierre Auger Observatory [1]. The techniques by which cosmic rays in a given energy range are detected depend critically on the flux at the time of arrival. In the energy range of $10^{11} - 10^{12}$ eV, the flux of cosmic rays is roughly 1 particle per square meter. This rate is high enough to allow for direct detection [2].

The atmosphere absorbs most of the cosmic rays, as it was demonstrated by Hess's original experiments. Radiation detected at ground level consist of secondary particles produced from interactions between primary cosmic rays and the air. To measure the primary cosmic rays directly, the detection equipment must be placed above the atmosphere. This is usually accomplished by carrying the instrument aboard high-altitude balloons flying at above 33,000 m, on Earth-orbit satellites, or in the future aboard the International Space Station (ISS). An example of a detector scheduled for deployment on the ISS is the alpha magnetic spectrometer (AMS), which is designed to search for nuclear antimatter in cosmic rays [2].At above $10^{15} - 10^{16}$ eV, the flux of cosmic rays drops to below one particle per square meter per year. This rate makes direct measurements impractical, as it would require flying very large detectors in order to collect sufficient number of particles. Hence a different method is required and radio techniques are one alternative which is explored in this work.

Extensive air showers

Over the last 70 years, physicists have studied cosmic rays with energies in excess of 10^{14} eV by using the Earth's atmosphere itself as part of the detection equipment. This technique takes advantage of the fact that interaction between high-energy cosmic rays and the air produces a correlated cascade of secondary particles. The process begins with the collision of the primary cosmic ray with a nucleus near the top of the atmosphere. This first collision of cosmic rays typically produces more than 50 secondary particles, a majority of which are pi-mesons (usually referred to as pions).

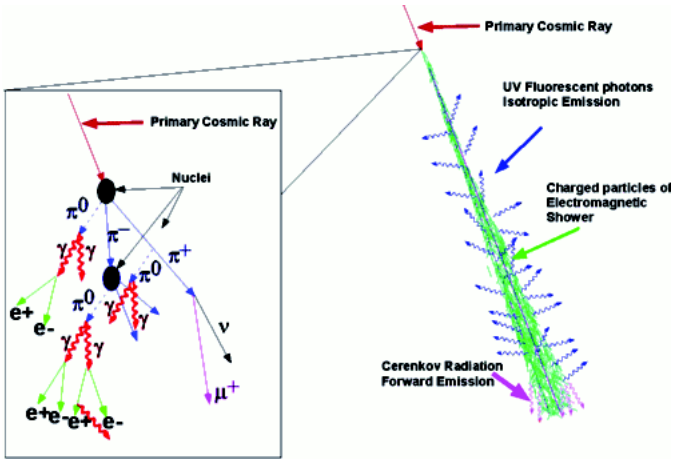

Figure 1.1: Extended air showers [2].

Pions come in three different flavors: positively charged, negatively charged, and neutral. All pions are unstable, but the charged pions are relatively long-lived and will most probably collide with another nucleus before decaying. The subsequent collisions are similar in nature to the primary collision. This process then leads to a cascade of particles which is referred to as a 'hadronic shower'. Figure 1.1 shows evolution of a shower.

One third of the produced pions are neutral. The neutral pions are very short-lived and almost all of them will decay into a pair of photons (gamma rays) before interacting with nuclei in the atmosphere. The photons interact with the nuclei in the air to produce electron-positron pairs, which in turn will produce photons via the 'bremsstrahlung' process. This cascading process leads to the formation of an 'electromagnetic shower'. The hadronic shower itself is continuously producing neutral pions and thus initiating secondary

electromagnetic showers along its path. High-energy cosmic rays are believed to consist mostly of charged nuclei. Gamma rays have been observed with energies as high as 10^{12} eV. In the case of a gamma-ray primary particle, the particle shower produced is purely electromagnetic. Generically, both types of cascades are called 'extensive air showers' (EAS).

Ground arrays

For air showers with energies in excess of 10^{15} eV, the shower maximum penetrates to half the vertical atmospheric depth or more. There is also sufficient number of particles in the cascade such that the remnant of the shower can be detected as a correlated event by an array or grid of individual particle detectors on the ground. The threshold (the lowest energy detectable by an instrument) of such 'ground array' depends on the altitude of the array. Typically, it is difficult to measure cosmic rays with energies below 10^{14} eV with ground arrays.

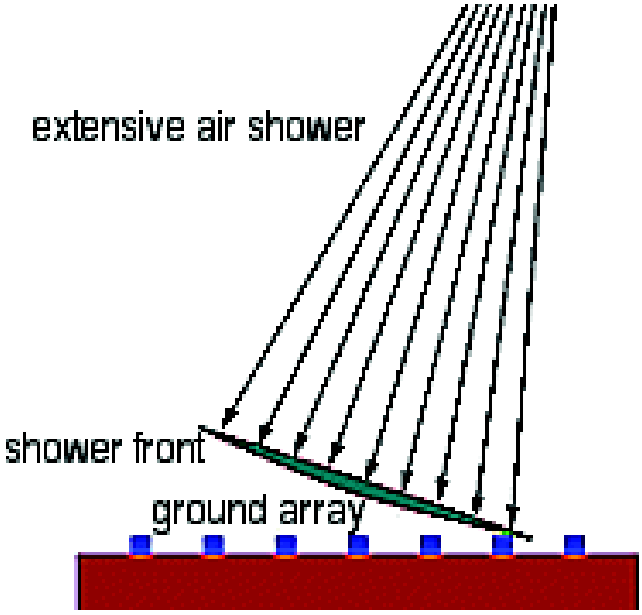

Figure 1.2: Schematic of ground array [2].

Figure 1.2 shows the schematic of a ground array. Each station of the array samples the density of particles in its neighborhood of the shower. The footprint of air showers usually extends hundreds of meters. The particles in

the air shower arrive in the form of a thin pancake traveling at essentially the speed of light. By measuring the time of arrival of the shower front at the individual stations, the direction of the primary cosmic rays can be calculated to about one degree accuracy [2]. Conventionally, the energy of the shower is deduced from r(600), the density measured at 600 m from the core of the shower at ground level. This density was chosen because it was the quantity which showed least amount of variations between different shower models [2].

Scintillation counters

Extensive air showers with many particles arriving on the ground can be detected with different kinds of particle detectors. Most common are scintillation counters, allowing to measure the time of arrival with high accuracy. Other common devices include water Cherenkov counters, resistive plate chambers and a variety of position-sensitive devices which allow to measure the particle direction. These tracking detectors include different types of drift chambers, streamer tube detectors, and Geiger tube detectors.

Hundreds of single particles arrive per square meter per second but extensive air showers are less common. Therefore, coincidences of several particle detectors are required. When looking for small showers with perhaps a few thousand particles, tens or hundreds of detectors separated by 10-30 meters are usually used. When looking for the much less frequent very large showers with billions of particles, the detectors can be placed at separations of about a kilometer to the next neighbor. The Telescope array project in Utah is meant to detect rare showers. They have 576 ground array detectors filling the area between three fluorescence sites and are set 1.2 kilometers apart from one another, covering an approximate area of 800 km^2.

Showers can be detected at even larger distances by the fluorescence light which is emitted by nitrogen molecules when charged particles are passing nearby. Imaging devices ('telescopes' with photomultipliers as cameras) can see the track of air showers through the atmosphere. This method was first used by the Fly's Eye experiment. Because the fluorescence light is very weak, only the most energetic showers can be detected this way. With similar light-sensitive devices, the more intense Cherenkov light of showers can be detected. Since the Cherenkov light is only emitted at a narrow angle to the shower axis, it can be seen only when being at most a few hundred meters from the shower axis [9].

Air Cherenkov arrays

Ground arrays sample the lateral density profile of the shower as it hits ground. No direct information is obtained for the longitudinal development of the shower. One way to supplement a ground array is to install a muon array. Another way is to implement an air Cerenkov array with the ground array. The particles in a typical air shower are all traveling just below the speed of light in vacuum. In air, however, they are actually traveling faster than the speed of the light in the medium. The result is that they emit light, called Cerenkov radiation, analogous to the sonic boom of a supersonic aircraft.

Atmospheric Cherenkov light

Charged particles moving through the atmosphere with a velocity larger than the local speed of light (the vacuum speed of light divided by the refractive index of the air) emit Cherenkov light. As shown in Figure 1.3 this light is emitted on a narrow cone around the direction of the particle. The opening angle alpha is a function of the density of the air and, thus, of the height of emission. It is increasing downward but is always less than about 1.4 degrees [3]. From each part of the particle track the Cherenkov light arrives on a ring on the ground. In an air shower, the initial particle interacts with the air atoms, producing many new particles. Most of those particles will be stopped or decay before they reach the ground. The Cherenkov light of all those shower particles travels faster than the local speed of light overlaps on the ground.[1]

The first to realize that cosmic-ray air showers would produce enough Cherenkov light to be detectable was Blackett in 1948 and the first to detect this light were Galbraith and Jelley in the early 1950s. Although there are other ways to detect air showers, the Cherenkov method has the lowest energy threshold among them. In the 1950s and 1960s the Cherenkov light was used to study properties of air showers induced by cosmic rays (protons and heavier atomic nuclei). Starting at about 1970, Cherenkov telescopes (for example the Whipple Gamma-Ray Telescope) were used to search for sources of TeV energy gamma rays. Although first detections were reported

[1]Different transliterations are in use for the name of the Russian physicist who (together with Vavilov) discovered the nature of this kind of light emission in 1934. In the literature, the effect is sometimes called the Vavilov-Cherenkov effect.

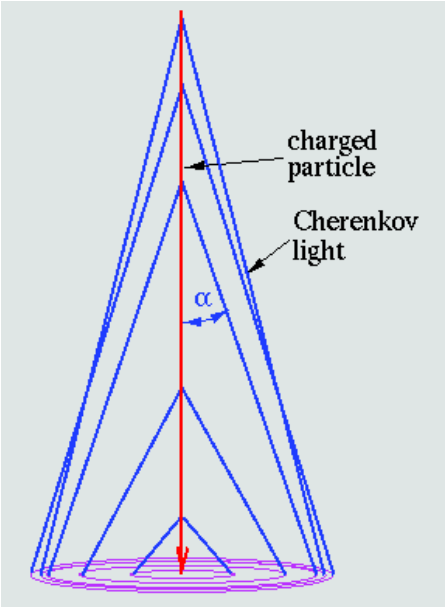

Figure 1.3: Cherenkov light [3].

in the 1970s, it was not before 1988 when the imaging technique provided the means to distinguish between cosmic-ray induced air showers (coming from all directions) and gamma-ray induced air showers. Only gamma rays, being responsible for a tiny fraction of all air showers, travel on straight lines through our Galaxy and can be used to image sources of such high-energy particles.

RADAR

The first experimental attempt to detect UHECR using radar was performed by Bernard Lovell and Patrick Blackett in the early 1950's. In Lovell's experiment, the observed signals were later interpreted as reflection from meteor trails. That was the birth of a technique today known as radio meteor scatter(RMS) [6][7]. This technique is explored in details in later sections.

1.2 Background of meteor detection

Meteor detection techniques can be broadly classified into two major categories as visual and radio techniques. The following section presents a brief overview of visual methods and details a description of the radio methods.

1.2.1 Visual and photographic techniques

Naked eye observations

For many years visual observations was the chief if not the sole, means of gathering information about meteors, much of it accumulated through the efforts of amateurs. These observations can provide vital information about meteors like magnitude, path position and shower or non-shower identification. Some of this highly desirable information can be obtained if the visual observer plots the meteor path against a star background. The plotting is done on a map on which few of the brighter stars and well-known constellations have been marked. Various projections have been used to transfer the celestial sphere to a plane. The most useful from the view point of meteor mapping appears to be the stereographic projection. Figure 1.4 shows one such map prepared by Millman for use near latitude 45°N [4].

The rocking mirror method

The method was developed by Öpik in 1934. In one arrangement the observer looked down on a plane mirror which rested face up on three ball supports. One of the supports was fixed and the other two, by means of a motor drive, were raised and lowered in simple harmonic motions, differing 90° in phase. The resultant conical motion at 10 rps causes the stars to appear as circles or ellipses as seen in Figure 1.5. Boothroyd devised a variation of the method in which the mirror rested on a single support and was given a conical motion of 30 rps by means of an eccentric shaft. With either instrument, a meteor moving across the field of view would appear to the eye to trace out a curve resembling a cycloid. The angular speed of the meteor may be deduced from the observed number of loops and the apparent length of trail [4].

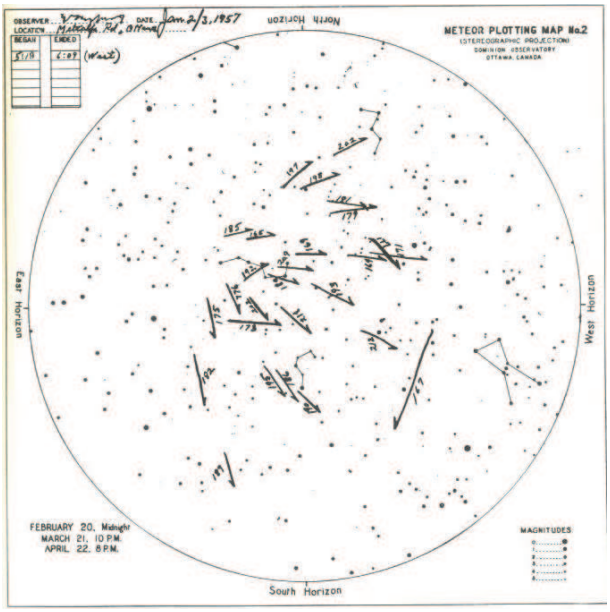

Figure 1.4: Star map with meteor paths plotted [4].

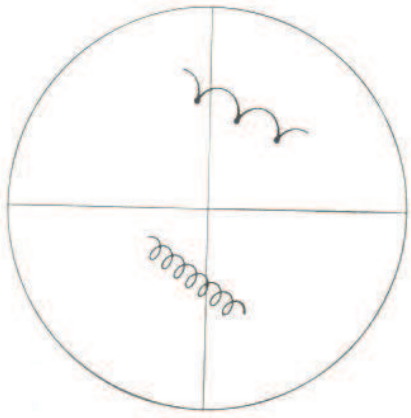

Figure 1.5: Sketch of meteor trails viewed in a rocking mirror.

Binoculars and telescopes

The limiting magnitude (measure of brightness) of stars which average eye can detect when aided by a telescope of aperture a is given by $M = 9 + 5log_{10}a$, where a is in inches [4]. The practical limit for detection of

telescopic meteors is about two magnitudes brighter than for stars; so we may write the limiting meteor magnitude as $M = 5log_{10}a$ where a is now expressed in millimeters. Typical rates with 50 mm binoculars are about three or four meteors per hour.

Small-camera photography

During clear nights direct photography can provide a permanent and accurate record of the luminous effects of the brighter meteors. Good quality 35-mm cameras yield quite acceptable photos and the technique is not difficult to learn. From the stationary camera one may determine the position of the meteor trail in azimuth, elevation, declination and also in right ascension if the exact time of the meteor is available. The limitation, of course, is that the average conventional camera will not record meteors fainter than zero or first magnitude.

Cameras with Schmidth optics

The Super-Schmidth camera, designed by Dr. Baker at Harvard University specially for meteor photography, has no peer in this field. The entire setup comprising of camera, equatorial mounting yoke, and drive system - standing 2.6 m high when mounted and weighed 3 tons. The aperture is 310 mm and the focal length is 203 mm. Cross sectional view of a super Schmidt camera is shown in Figure 1.6.

Meteor spectrophotography

Most of the conventional cameras may be converted to spectrophotographs by placing in front of the lens either a glass prism with an angle of about 30° or a transmission grating ruled with 80 to 400 line/mm and designed to concentrate most of the light into the first-order spectrum. The average sensitivity of a spectrographic camera will be about two magnitude brighter than that of the same camera without the dispersive device, partly because of additional losses in the dispersive medium but mainly because the light is divided among several monochromatic lines.

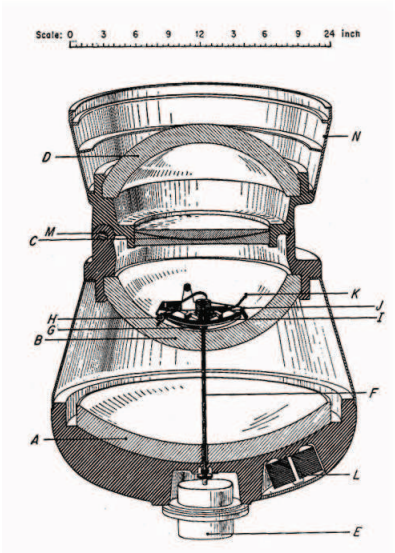

Figure 1.6: Cross sectional view of Super-Schmidt camera. (A) Main mirror (B) Rear glass shell (C) Correcting plate (D) Front glass shell (E) Shutter motor (F) Shutter shaft (G) Rotating shutter (H) Focusing post (I) Film holder (J) Film holder hinge (K)Vacuum line (L) Counter weight (M) Hinge for opening camera (N) Dew cap [4].

Photoelectric observations

The high-speed response and the potential sensitivity of photoelectric devices offer several attractive possibilities for the trapping of elusive and transient meteor. A few meteors as faint as third magnitude were recorded by the photocell system, though the practical working limit appeared to be about the second magnitude. Most of the noise background in the photocell output was due to star scintillations and other random light variations.

1.2.2 Radio techniques

Radio techniques can be classified in two major groups as back scatter and forward scatter. The basic difference between the two techniques is the location of the receiver. As seen in the Figure 1.7 in case of backscatter radar transmitter and receiver are placed close to each other. In case of

forward scatter the transmitter and receiver are at a much greater distance covering a much larger area as seen in Figure 1.8.

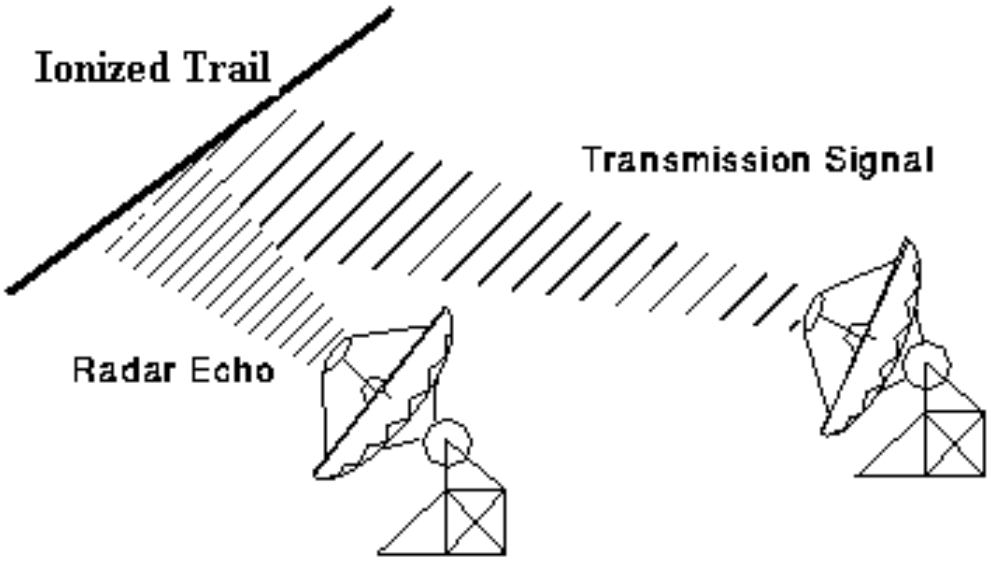

Figure 1.7: Back scatter.

Another desirable factor in favor of a forward scattering system is its passive nature. The receiver is tuned to a transmitter below the horizon or at a distance larger than its line of sight range. Since the transmitter transmits signals for its own purpose the reflected residual power is used for detection. In case of meteor burst communication the distant transmitter is used to send encoded message signals but for meteor detection a distant television transmission serves the purpose. The advantage of the backscatter technique is the control of the transmitter. Since the signals can be modeled specific to the application,the received patterns can be studied in details. Forward scatter is the method adopted for detection in the proposed Data Acquisition system (DAQ) due to its advantages.

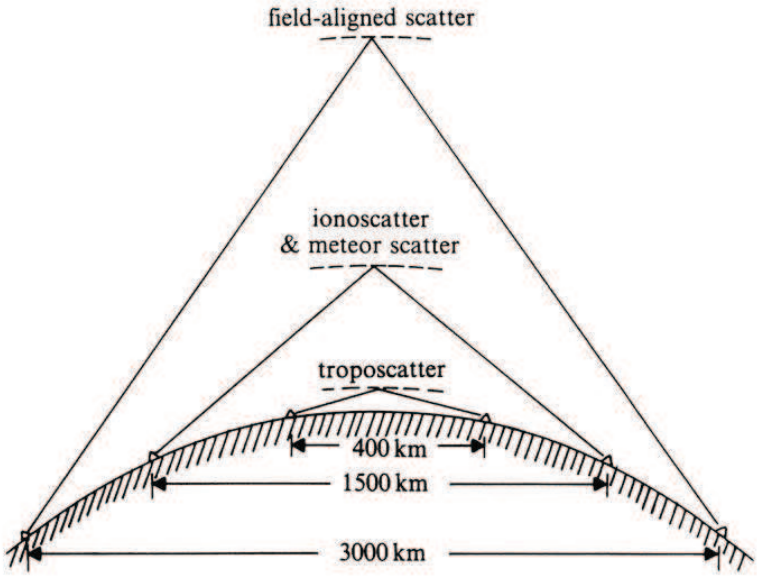

Figure 1.8: Forward scatter.

1.3 Forward scattering for UHECR detection

1.3.1 The physics of UHECR trails

UHECR with energy $E > 10^{18}$ eV can produce ionization densities in excess of 10^{13} m^{-1} that will reflect electromagnetic waves with frequencies between 50 to 200 MHz. The reflection is likely to take place near the shower core because particle densities in EAS fall obeying a power law as function of the distance from the shower center. In the absence of a dense atmosphere the reflection of the electromagnetic waves from EAS would be described using the same formalism as used for radio meteor scatter (RMS). However, EAS takes place at lower altitudes where the higher air density and electronegative O_2 attenuate the reflected signal and shorten the lifttime of the ionization cloud. The length of the reflective column is determined by two factors: the longitudinal shower thickness and the free electron lifetime. The shower thickness near the shower axis is small being at most 3 m wide. Therefore the free electron lifetime determines the length of reflecting column. The exact lifetime of free electron depends on the conditions under which ionization is created.

1.3.2 Forward scatter for meteor detection

Radio detection of meteors was first suggested by H. Nagaoka, and confirmed by Pickard and Skellett in the 1930s. Unlike UHECR, the ionization trails are produced by direct collisions between air molecules and ablated materials from a meteor's surface which contains atoms with kinetic energies of 10^2-10^3 eV.

Typical radio detectable ionization trails produced by meteors occur at a height of 80-120 km. The majority of meteors that can be observed by radio techniques are sub visual and their velocities approaching the Earth are between 11 km/s (escape velocity from the Earth) and 72 km/s (escape velocity from the solar system). Based on electron density, two major classes of meteor trails have been identified: underdense and overdense trails. The low electron density of underdense trails allows the incident wave to pass through. This phenomenon allows the trail to be considered as an array of independent scatterers. Overdense trails are those wherein the electron density is high enough to prevent complete penetration of the incident wave and to cause reflection of waves in the same sense that the ordinary ionospheric reflections occur. There is no clear distinction between overdense and underdense trails but usually a line density of about 10^{14} electrons/m is considered as a transition line.

The forward scattering radar system is also called bistatic radar. A bistatic radar does not require a dedicated transmitter, and thus is very cost efficient. The geometry in a forward scattering scenario can be visualized as in Figure 1.9 [5]. For this geometry, the power of received radio signals scattered from underdense meteor trails can be formulated as 1.1[18]

$$P_R(t) = \frac{P_T G_T G_R \lambda^3 q^2 r_e^2 sin^2\alpha}{16\pi^2 R_T R_R (R_T + R_R)(1 - cos^2\beta sin^2\phi)} exp\left(\frac{8\pi^2 r_0^2}{\lambda^2 sec^2\phi}\right) exp\left(\frac{-32\pi^2 Dt}{\lambda^2 sec^2\phi}\right) \tag{1.1}$$

where the parameters have the following meaning:

P_T	transmitted power
G_T, G_R	transmit and receive antenna gains as a function of location
q	electron line density in the trail (e/m) assumed uniform along the trail
D	diffusion constant, a function of trail height (m^2/s)

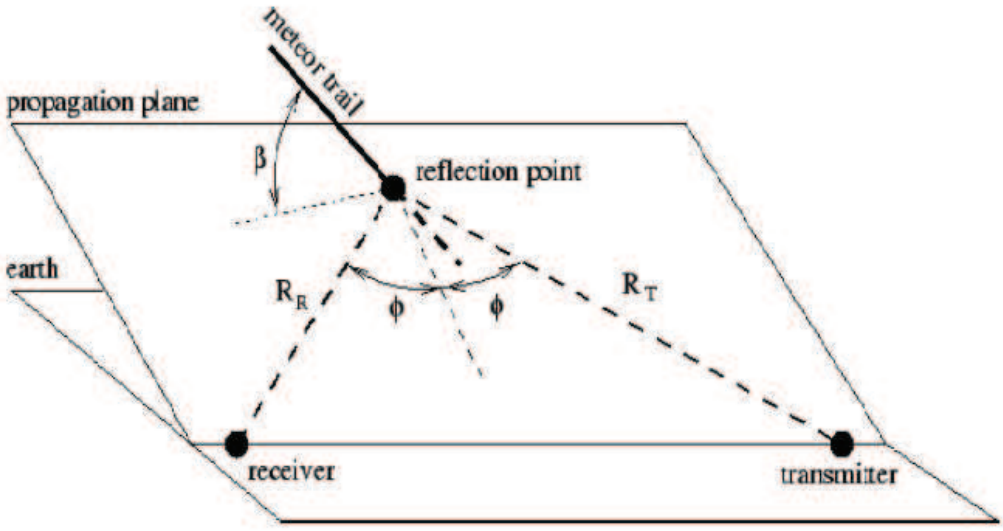

Figure 1.9: Forward scatter geometry [5].

λ	wavelength (m)
r_e	classic radius of electron ($2.818 \times 10^{-15} m$)
R_T, R_R	distances (m) from transmitter and receiver,respectively, to the center of first Fresnel zone
r_0	initial effective trail radius (m)
α	angle between the incident electric field and the wave normal from the receiver to the trail
2ϕ	angle of incidence formed by the vector $\vec{R_T}$ and $\vec{R_R}$
β	orientation of the trail in the plain normal to the plane of incidence containing $\vec{R_T}$ and $\vec{R_R}$

For the same geometry and using the same notation, the received power of radio signals scattered from overdense meteor trails can be formulated as

$$P_R(t) = \frac{P_T G_T G_R \lambda^3 q^2 r_e^2 sin^2\alpha}{16\pi^2 R_T R_R (R_T + R_R)(1 - cos^2\beta sin^2\phi)} \left(\frac{4Dt + r_0^2}{sec^2\phi} \ln \left(\frac{r_e q \lambda^2 sec^2\phi}{\pi^2 (4Dt + r_0^2)} \right) \right) \tag{1.2}$$

Figure 1.10 illustrates a 2-D geometric scheme with $\alpha = 0$ and $\beta = 0$.

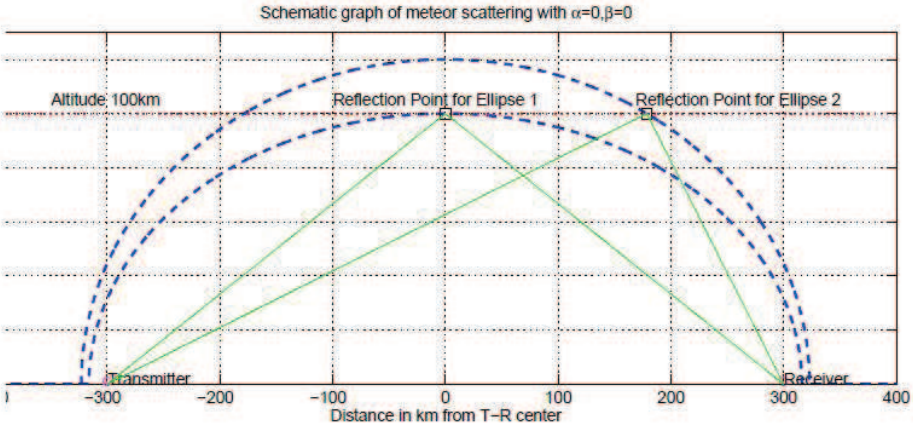

Figure 1.10: 2-D schematic for $\alpha = 0, \beta = 0$ [5].

1.4 Objectives and contribution

The main objective of this work is to propose a time synchronized DAQ system with a robust detection algorithm for cosmic ray detection.

We present the underlying physics of cosmic rays and establish a well defined problem statement in the signal processing domain. We present the idea to the signal processing community in form of a publication [7], which was well received by the community as an innovative application. This work is also a compilation of many ideas proposed since the Second World War. The work presents solutions implemented and questions that arose during development of the proposed DAQ.

With the motivation of cost efficiency, different antenna designs were tested and finally the most effective and cost efficient antenna design was proposed for future use.

The core revelation of this work is the performance analysis of different commercially available radio receivers. During this analysis the operating system-based factors, hardware performances, programmability, spectral flexibility and other data related parameters were studied. Finally the open source software defined radio GNU Radio was proposed as the reliable component.

Selection of GNU radio presented an excellent opportunity to explore the world of software defined radio. Although this work presents only the relevant part of radio processing involved, we studied intriguing C++ and

Python operational codes which transformed the signals to the data format we needed. This effort enabled us to write software codes which could precisely perform tasks making the system more desirable. This insight also enabled us to compress the data to great degree providing a possible feature of network data acquisition to a central storage server.

After a lot of uncertainty regarding the multiple site synchronization issue, we were finally able to design a cost efficient time synchronization scheme. Although the scheme could not be implemented in field due to time constraints, the crucial test results were precise enough to assume its success whenever implemented.

The signal processing algorithms developed till date are efficient enough to segregate all the candidate events. Preliminary test results show the expected meteor activity patterns [7].

Finally, with the simultaneous data recording at Ross High School and Custer Institute, we were able to demonstrate the autonomous operation, portability, cost efficiency and easy maintainability features of the DAQ, which were some of the primary motivations behind this effort.

The remaining of this document is organized as follows:

The second chapter provides an overview of the DAQ. Initially the entire setup is presented and then individual components are explained. The basic antenna requirements and associated electromagnetics are explained in brief. The selection criterion and relevant features of the radio receivers used till date are mentioned. The section concludes with a discussion of the challenges and possible solutions to the problems related to the antenna design and receiver selection.

The third chapter is completely dedicated to GNU Radio. After experimenting with different models for receivers, GNU Radio was found to provide the best performance and feature match for the proposed DAQ. Hence the work presents a detailed description about GNU Radio operation. The desirable features and advantages compared to other radios are also discussed. Although GNU Radio fulfills many criteria required by DAQ, it also presents some additional challenges. These challenges and possible workarounds conclude the chapter.

The fourth chapter focuses entirely on the signal processing. The time synchronization, detection algorithm and localization are discussed in detail. This chapter also presents some results of the data analysis done till date under the MARIACHI experiment.

The fifth chapter comprises of the conclusion and suggestions for future

work.

Chapter 2

Data acquisition system

The idea of radio detection of cosmic rays was proposed in the early 1940s. Since then many different techniques have been tried and tested. The goal of radio detection is to estimate the direction of arrival, hence the ideal setup will be a grid of at least four synchronized stations. The DAQ proposed in this work is a prototype of one radio station which can be treated as a node of the grid. The concept of grid as shown in Figure 2.1, is similar to the idea of ground arrays of particle detectors. The following sections give the system overview and discuss the individual modules of the DAQ in detail.

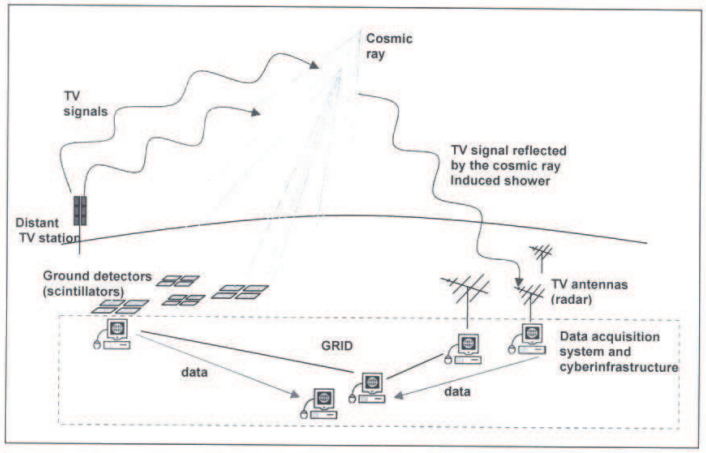

Figure 2.1: The concept of grid of radar stations [6].

2.1 DAQ: System overview

The Mixed Apparatus for Radar Investigation of Atmospheric Cosmic-rays of High Ionization (MARIACHI) [9] experiment at State University of New York at Stony Brook uses a prototype of the proposed system. The currently operational DAQ is used for detection of meteors as a proof of concept.

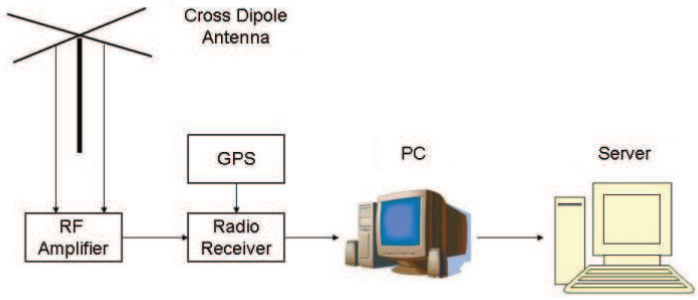

Figure 2.2: DAQ setup.

The receiver uses a cross dipole antenna. A cross dipole antenna is formed by placing two Hertzian dipoles perpendicular to each other. The detailed analysis of the antenna is provided in the next section. For detection of forward scatter signals a very high frequency (VHF) television broadcast station is utilized at the transmitter. The frequency range chosen by the MARIACHI setup is 54-88 MHz, which is allocated to channels 2-6 by the Federal Communications Commission (FCC). Although this frequency restriction is not necessary for meteor scattering, it may be required to ensure detection of signals scattered from ionization trails generated by UHECR. A specular reflection from an electron cloud only happens when the minimum free electron density is reached [18]. This is given by:

$$\nu_p = \sqrt{\frac{n_e e^2}{\pi m_e}} \tag{2.1}$$

where $n_e = 3.8 \times 10^{13} m^{-1}$ for $f = 55.24$ MHz (channel 2) and $n_e = 5.6 \times 10^{13} m^{-1}$ for $f = 67.26$ MHz (channel 4). When the minimum free electron density is reached the electron density is high enough so that the

electrons re-radiate energy from their neighbors. This happens in meteor trails and is usually called an overdense regime. The converse is the underdense regime and there is no re-radiation by electrons in the cloud instead total reflection takes place.

2.1.1 Television spectrum

Since the early days of experimental television broadcasting, the choice of the carrier frequency has been largely dictated by the availability of space in the spectrum. Frequencies below 42 MHz were completely devoted to other services when the television allocation was set by FCC in August 1936. At that time, the experience with frequencies above 300 MHz was so meager that no channels above 294 MHz were considered. When commercial broadcasting started in June 1941, 19 very high frequency (VHF) channels were authorized, but this allocation was reduced to 12 channels, between 54 and 216 MHz. In 1951 the increase in demand for television service resulted in a proposal to allocate 70 additional ultra high frequency (UHF) channels between 470 and 890 MHz [8].

Other than availability and economic factors dictating the choice of television carrier frequency was the special property of frequency range from 50 to 1000 MHz. The waves in this region of the spectrum primarily propagate by the ground wave component which limits reliable transmission to the radio horizon. This property enables the reuse of spectrum at distances greater than the line of sight. The frequency range is also advantageous because the fading is not as pronounced as at lower frequencies, and the level of natural atmospheric disturbances is low. But man made interferences from electrical contacts and ignition systems are more prevalent, particularly in the range from 50 to 200 MHz, than at lower frequencies.

Refraction of the waves in the upper atmosphere (ionosphere) is rare, so that it eliminates the possibility of long distance propagation by ionospheric sky. Refraction in lower atmosphere (troposphere) occurs more often and accounts for sporadic transmissions. These properties make the television signal a good candidate for the forward scattering radar model. The attenuation of the ground wave becomes more pronounced as the frequency increases.

The picture signal is transmitted using the amplitude modulation scheme (AM). In conventional AM, two sideband frequencies are generated for each modulating frequency. These sidebands appear symmetrically above and

below the carrier frequency, each sideband at a separation numerically equal to the corresponding modulating frequency. Since the maximum modulating frequency (in the American system) does not exceed 4.5 MHz, it follows that the maximum extent of the sideband structure is $2 \times 4.5 = 9$ MHz. Since the region of spectrum needs to be used efficiently another technique of modulation is employed.

The means of sideband reduction universally used in broadcast service is the vestigial sideband system illustrated in Figure 2.3. This system is based on the fact that all pairs of sideband components, associated with a given modulating frequency, contain identical information. It is theoretically possible, therefore, to suppress in a filter one set of sidebands, thus halving the sideband content of the signal, without any loss of picture information. When this theory is put into practice, it is found to be impractical to completely suppress one set of sidebands, because the phase shift associated with the filter cutoff produces excessive distortion when applied to the low frequency sidebands adjacent to the carrier [8].

The compromise adopted in practice is to transmit at full amplitude both sets of sidebands within 0.75 MHz of the carrier, while suppressing completely all the frequencies in the lower sideband, farther than 1.25 MHz from the carrier. The transmission of a "vestige" of the lower sideband accounts for the term "vestigial sideband" transmission. One disadvantage of the vestigial sideband transmission is the introduction of phase and amplitude distortion even with ideal response curves at the transmitter and receiver.

The MARIACHI setup is tuned to television channel 4 positive offset transmission frequency of 67.26 MHz. The antenna provides data from two separate dipoles. To improve the received signal quality and compensate the cable losses a pre-amplifier is used. Both channels are fed to the radio receiver through a pre-amplifier of known gain.

From the RF amplifier the data is fed to a radio receiver. The basic function of the radio receiver is to filter out the desired part of the signal from a very wide spectrum of the TV signal.[1] The spectrum of the TV signal is shown in Figure 2.3.

Most of the power of TV signals is concentrated around the video carrier frequency. The audio component of the TV signal is modulated using frequency modulation (FM). The 15.75 kHz and 60 Hz harmonics around

[1]The FCC standard features of US TV broadcast signals can be found at the official website of FCC [19].

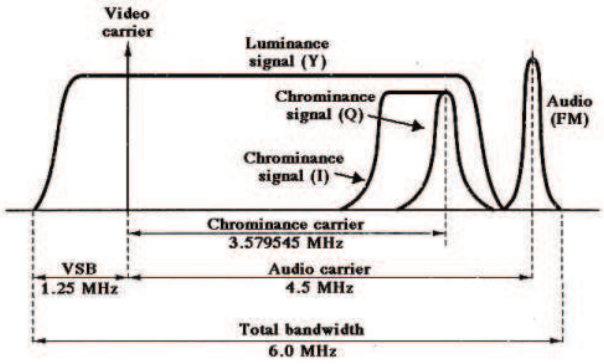

Figure 2.3: The spectrum of NTSC TV signal [7].

the video carrier in the spectrum result from the horizontal and vertical scan frequencies. The entire spectrum can be considered as a random signal due to the continuous variation of the picture (video) content. For detection of meteors a narrow band receiver is sufficient, since the meteor echo durations range from 0.1 s to several minutes. However much wider bandwidth ($>$ 10 kHz) is required for detecting UHECRs because of their much shorter lifetime ($<<$ 0.1 ms).

After the filtering is completed by the radio receiver the data is transfered to the computer via universal serial bus (USB) or sound card depending on the type of radio receiver used. Finally after the data are stored on the computer they can be processed offline or transfered to the remote server depending on the requirements.

2.2 Antenna

A dipole antenna, developed by Heinrich Rudolph Hertz around 1886, is a type of wire category of antennas that can be made by a simple wire, with a center-fed driven element for transmitting or receiving radio frequency energy. Since the antenna has two elements it is called a dipole. When the length of antenna is equal to half of the tuning wavelength, it is called as half dipole as shown in Figure 2.4. The antenna is the core element of the receiver module. The basic requirements of the antenna are its ability to receive the

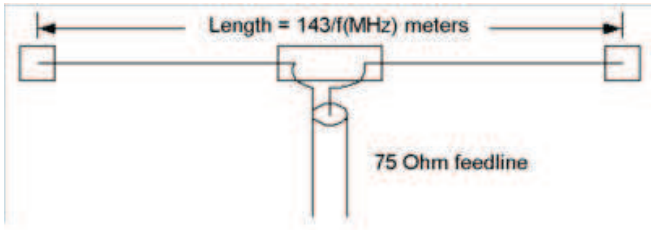

Figure 2.4: A half dipole antenna [8].

scattered signals from the ionized trails and provide some vital information about the polarization of the received signals. Another important factor in the case for antenna selection is its radiation pattern.

The radiation pattern of an antenna is the plot of its transmitted energy in all directions. The pattern gives a measure of directivity of the antenna. The two dimensional radiation pattern of a half dipole is as shown in Figure 2.5. And the three dimensional pattern can be seen in Figure 2.5. It can

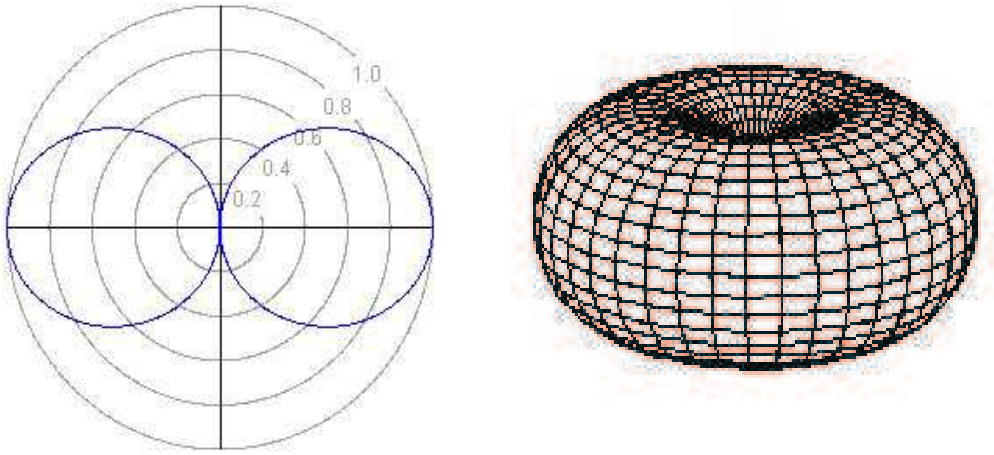

Figure 2.5: 2D representation of the vertical cross section (L) and 3D (R) radiation pattern of single dipole antenna [9].

be seen from the radiation pattern that the antenna has a negligible gain at 90°. To overcome this issue another model called cross dipole is used in some applications. The antenna model used in MARIACHI is a cross dipole. Basically a cross dipole antenna is constructed by mounting two half dipoles perpendicular to each other on the same stand. The resultant radiation

pattern is as shown in Figure 2.6.

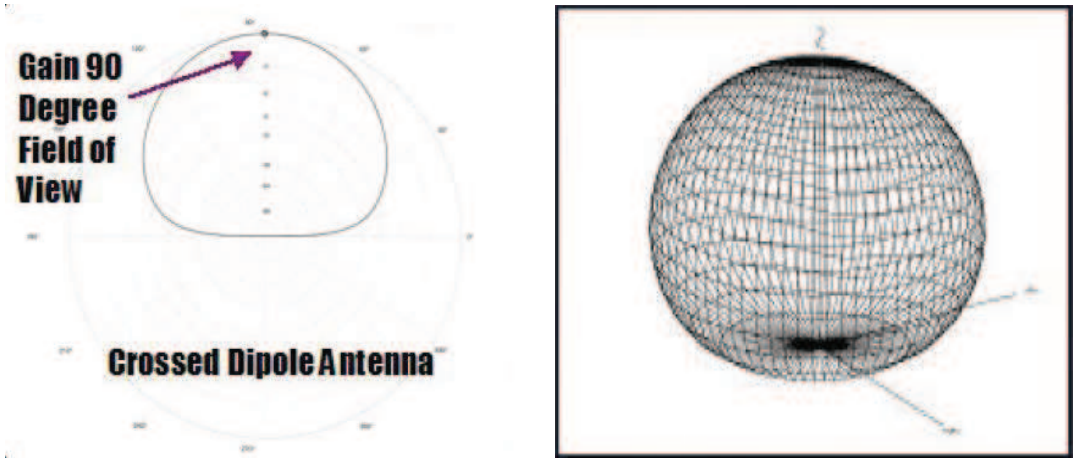

Figure 2.6: 2D (L) and 3D (R) radiation pattern of cross dipole antenna [9].

2.2.1 Transmission path of signals

The forward scatter radar is heavily dependent on the geography of the transmitter and receiver. For the forward scattering to work the knowledge of visual (line of sight) and radio horizon is essential. The spherical surface of the Earth blocks both direct- and surface-reflected components at the horizon. Since the horizon plays such an important part in limiting propagation, it is important to compute these distances. The two main distances of interest are visual horizon and radio horizon. The visual horizon is as seen by eye from the transmitting radiator and the radio horizon is the locus at which the radio waves (which follow curved lines) falls tangent to the surface.

The visual horizon can be computed from the right triangle in Figure 2.7, in which r_v is the horizon distance, h the height of the radiator above the surface, and R the actual radius of the Earth. Upon simplification and neglecting the square of the antenna height, we obtain

$$r_v{}^2 = 2Rh \tag{2.2}$$

When h is taken in feet and the mean radius of the Earth (3956 miles) is substituted, the equation becomes

$$r_v = 1.22\sqrt{h} \quad miles \tag{2.3}$$

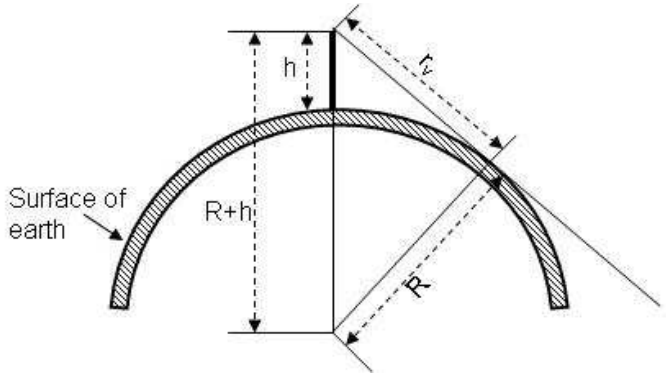

Figure 2.7: Visual horizon [8].

The radio horizon must be computed on the basis of the curved ray shown in Figure 2.8. The wave path is curved because the refractive index of the atmosphere decreases with height owing to decrease in pressure and moisture content. This causes the ray to be curved downward as it travels over the surface. The distance of the radio horizon with its modified geometry can be computed as follows

$$r_r = 1.41\sqrt{h} = \sqrt{2h} \quad miles \tag{2.4}$$

2.3 The radio receivers

The main function of the radio receivers is to selectively filter the received TV signal. The bandwidth of a TV signal for a single channel is 6 MHz. To increase the efficiency of the system the irrelevant spectral information is discarded. In case of cosmic ray detection a bandwidth of 10 kHz around the distant carrier is needed and for meteors 2 kHz is sufficient. To achieve flexibility in changing the radio parameters software defined radios (SDRs) are preferred.

A software-defined radio is characterized by its flexibility. By simply modifying or replacing software programs can completely change its functionality. This allows easy upgrade to new modes and improved performance without the need to replace hardware. An SDR can also

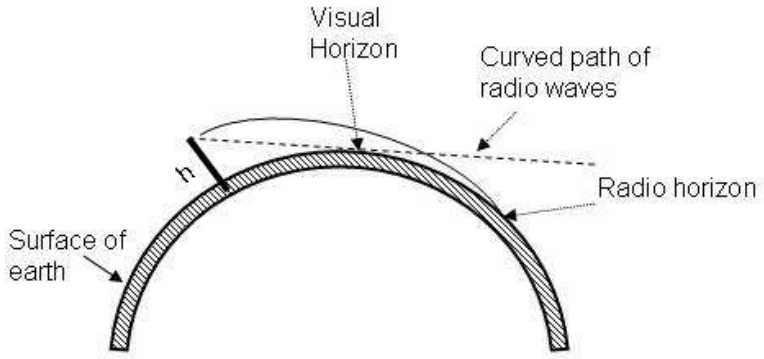

Figure 2.8: Radio horizon [8].

be easily modified to accommodate the operating needs of individual applications. There is a distinct difference between a radio that internally uses software for some of its functions and a radio that can be completely redefined in the field through modification of software. The latter is a software-defined radio. Many of these designs incorporate mathematical functions into hardware to perform all of the digitization, frequency selection, and down-conversion to baseband. To achieve flexibility of frequency tuning and gain control, SDRs are preferred. The basic structure of a software defined radio is as shown in Figure 2.9. The input to the SDR hardware is the signal from the antenna which is analog in nature. The analog signal is digitized by the analog to digital (A/D) converter in the SDR. Then the digital output is frequency translated to baseband and further signal processing is done. The detailed analysis of SDR is presented in the next chapter.

The SDR software is installed on a computer. The hardware can be either connected to a PC mother board using a data bus (WinRadio) or via universal serial bus (USB) port (GNU Radio, PCR1500). The user interface for PCR1500 and Winradio are shown in Figure 2.10 and Figure 2.11 respectively,[2]. In the case of GNU Radio the parameters of the receiver have to be entered as inputs to a Python code or script.

The parameters of interest are:

[2]The specifications of Winradio, PCR1500 can be found in [12] and [11].

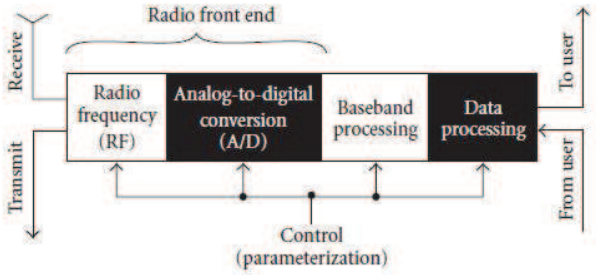

Figure 2.9: Basic Structure of SDR [10].

Figure 2.10: iCom PCR1500 user interface [11].

- Intermediate Frequency (IF) bandwidth: The IF bandwidth is the main parameter of interest as it allows the system to extract only the relevant part of the wide TV spectrum. In the case of meteors, 1 kHz bandwidth is sufficient and for cosmic rays a bandwidth greater than 10 kHz is required. For MARIACHI [9], the center frequency of the band is 67.26 MHz, which is the carrier frequency of the selected TV stations below the horizon.

- Receiver gain: The gain allows to compensate for the antenna and cable losses. It also depends on the volume settings of the computer if the SDR hardware is connected to the sound card of the controlling computer.

Figure 2.11: Winradio user interface [12].

- Recording frequency: This is the center frequency of the band of interest.
- Sampling rate: This decides how many digital samples are collected per second or the rate at which samples are acquired. Since the input to the SDR is analog and the output is digital, the sampling rate is a critical factor. Insufficient sampling rate means that the IF bandwidth is limited to the half of sampling rate (Nyquist criterion). However, in practice, the IF bandwidth is much lower than half of the sampling rate.

2.4 Data acquisition module

The output of the SDR is stored on the host computer in form of files with extensions '.wav' and '.txt' (Winradio, PCR1500) or binary format (Gnuradio). Initially the data are always stored on the local hard drive. The data recorded in the '.wav' files are continuous in the sense that all the sampling points are recorded. In '.txt' files the average signal and noise power over 0.1 s are recorded. The processing of text files is much faster compared to wave files but yields lesser information in terms of frequency content of the signal. From the local memory the files can be transfered to the server using secure shell (SSH) or by manually removing the local hard disk and connecting it to the server. The file size depends on the sampling rate set during the recoding of the data. After the data have been recorded,

they can be accessed later and can be processed offline using Matlab.

2.5 Challenges

- Antenna
  - The antenna is always vulnerable to receiving reflections due nearby structures.

    Initially the test setups at Stony Brook University and Brookhaven National Lab suffered this problem. To overcome this problem, the setups were shifted to remote locations (Custer Institute, Southold (Long Island, NY) and Ross High School, East Hampton (Long Island, NY)), which are less populated regions of Long Island. Moving away from urban location also reduced the electronic noise contribution to the noise floor.
  - Being omni directional the antenna covers a very wide area of sky at the same time. In case of meteors this could be a problem since there is a possibility of multiple events in different directions at the same time. Also omni-directional antenna picks up more noise due to its increased reception area.

    A possible solution is to use multiple highly directional antennas at a single site. Then their synchronization is a problem. In this work signal processing algorithms are used to detect multiple events and combat increased noise.
  - Again due to omni-directionality the antenna is capable of receiving many different distant stations at the same time. This creates a problem if a strong local carrier exists. Although the local carrier operates at a frequency offset of $\pm$ 10 kHz, it is still strong enough to create local reflections at the distant carrier frequency.

    Currently, the implemented solution is filtering only the band of interest from the received signal. However just filtering alone is not enough for complete elimination of local signal reflection.
- Radio receivers

- The parameters defined by software in SDR can be translated inaccurately in hardware.

  This issue becomes significant only in scenarios where the exact energy of an event is calculated. Currently all the data processing activities are independent from that parameter.

- In Windows-based systems there is no access to the software code and hence no modifications are possible.

  Using the GNU Radio development kit and the Linux operating system, this problem was solved. The Linux system includes higher interaction with code, and at the same time it gives a greater insight of the hardware operation.

- If the PC sound card is involved in the data recording process, there is always a problem of data loss due to inaccurate sampling frequency. This problem arises because of a low quality local oscillator used in PCs.

  With the use of GNU Radio and its corresponding hardware, the PC sound card is completely bypassed. The detailed operation of hardware is explained in the next chapter.

• Data acquisition module

- The time stamping of files is done using the PC clocks. Since the clocks are not very accurate, external time synchronization mechanisms have to be employed to ensure that the data from all sites are coherent. Detailed time synchronization schemes are proposed in Chapter 4.

- Continuous recording of data demands a huge disk space. While recording with Winradio using 22,050 sampling frequency and 2kHz bandwidth, the needed average disk space was 8 Giga bytes for 24 hours. Even larger memory is required for cosmic rays when higher sampling rates are used. This problem will exist until a reliable processing algorithm is tested with all kinds of data. Since currently the system is in an experimental stage, no data can be discarded without a detailed analysis.

- Even though in future the data transfer will be automated, it will heavily depend on the Internet connection.

– Currently the system processes the data offline but ultimately it should be able to process data in real time. Real time processing would require more computing power and a pre-filtering of samples to ensure only relevant data get recorded.

Chapter 3

Radio receivers

3.1 Introduction

Software radio is a methodology of getting the code as close to the antenna as possible. Doing so turns radio hardware problems into software problems. The fundamental characteristic of software radio is that software defines the transmitted waveforms, and software demodulates the received waveforms. This is in contrast to most radios in which the processing is done with either analog circuitry or analog circuitry combined with digital chips.

Software radio is a revolution in radio design due to its ability to create radios that change on the fly, creating new choices for users. At the baseline, software radios can do pretty much anything that a traditional radio can do. The exciting part is the flexibility that the software provides us. Controlling a computer with necessary hardware support makes experimenting with radios easier, interesting and attractive.

3.2 GNU Radio - Overview

GNU Radio is a free software toolkit for learning about, building and deploying software radios. GNU Radio provides a library of signal processing blocks and the glue to tie it all together. It is free and open source, it comes with complete source code so anyone can look and see how the system is built. The receiver path of GNU Radio is

Antenna− > Analog front end− > ADC− > Software code

The experimental setup for MARIACHI experiment will be considered for explaining the operation of GNU Radio.

3.2.1 Universal Software Radio Peripheral (USRP) board

GNU Radio is reasonably hardware independent. Regarding the Radio Frequency (RF) front end and Analog to Digital Converters (ADC) and Digital to Analog Converters (DAC), there are certainly many choices. The USRP board is designed for GNU Radio. The availability of all features and a readily available support by the GNU Radio community make USRP an obvious choice of hardware. The schematic of the USRP board is shown in Figure 3.1

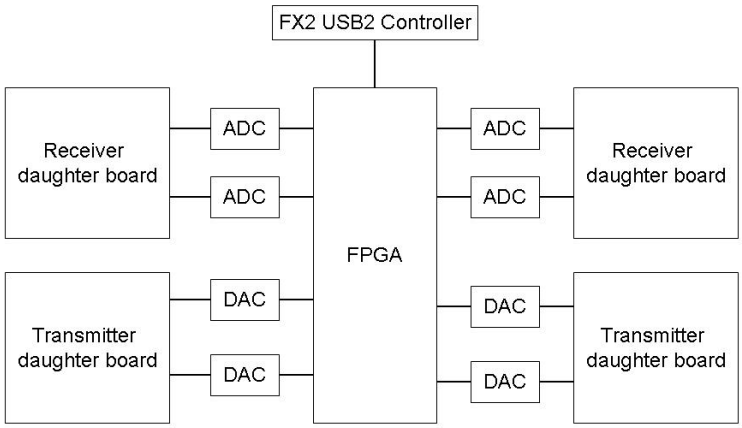

Figure 3.1: Schematic of USRP board.

AD/DA Converters

There are four high speed 12-bit AD converters. The sampling rate is 64 MS/s. In principle, an ADC can digitize a band as wide as 32 MHz. If we sample a signal with an intermediate frequency (IF) larger than 32 MHz, we introduce aliasing and actually the band of the signal of interest is mapped to some places between -32 MHz and 32 MHz. Sometimes this can be useful. The higher the frequency of the sampled signal, the more the SNR will be degraded by jitter. The recommended upper limit is 100 MHz.

The full range of the ADCs is two volt peak to peak, and the input is 50 Ω differential. This corresponds to 40 mW, or 16 dBm. There is a Programmable Gain Amplifier (PGA) before the ADCs to amplify the input signal to utilize the entire in-out range of the ADCs, in case the signal is weak. The PGA is up to 20 dB. The available rates of sampling are all multiples of 128 MHz, such as 64 MS/s, 32 MS/s, 25.6 MS/s and 21.33 MS/s.

The ADC used in the system is the part of the mixed-signal front-end processor AD9862. The functional block diagram of the ADC chip is shown in Figure 3.2 [13].

Daughter boards

There are slots for two transmitter (TX) daughter boards, labeled TXA and TXB, and two corresponding receiver (RX) daughter boards, RXA and RXB on the USRP motherboard. Each daughter board slot has access to two of the four high speed AD/DA converters (DAC outputs for TX, ADC inputs for TX). This allows each daughter board which uses real sampling to have two independent RF sections, and two antennas (four total for system). If complex in-phase quadrature (IQ) sampling is used, each board can support a single RF section, for a total of two for the whole system. In the meteor detection setup the TV receiver (TVRX) daughter board is used. The TVRX daughter board is equipped with Microtune 4937 cable modem tuner.[1]

Field Programmable Gate Array (FPGA)

FPGA plays a key role in the GNU radio system. The basic function of the FPGA is to perform high bandwidth math and to reduce data rates

[1]For technical specification refer to Microtune TUNER 4937 DI5 3x7901 datasheet. The production of this model has been discontinued but the data sheet could be requested from their website [20].

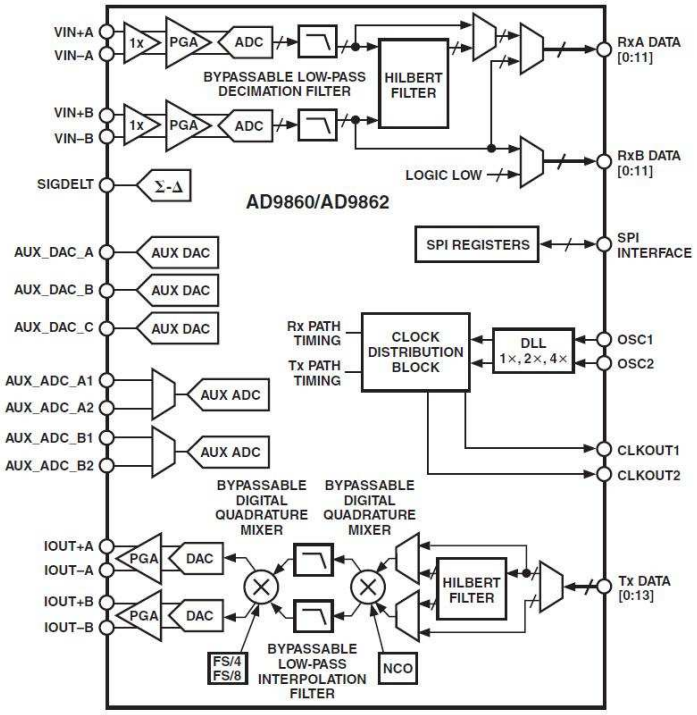

Figure 3.2: Functional block diagram of AD9862 [13].

compatible with USB 2.0. The FPGA connects to a USB interface chip, the Cypress FX2. FPGA circuitry and USB Micro-controller are programmable over a USB2 bus.

The standard FPGA configuration includes digital down converters (DDC) implemented with cascaded integrator-comb (CIC) filters. CIC filters are very high performance filters using only adds and delays. The FPGA implements four DDCs. This allows one, two or four separate RX channels. At the RX path, there are four ADCs and four DDCs. Each DDC has two inputs I and Q. Each of the four ADCs can be routed to either of the I or Q input of any of the four DDCs. This allows for having multiple channels selected out of the same ADC sample stream. The multiple RX channels

(one, two or four) must all be at the same data rate (i.e. same decimation ratio). The entire receiver path of the USRP is shown in Figure 3.3 and a block diagram of the DDC is shown in Figure 3.4.

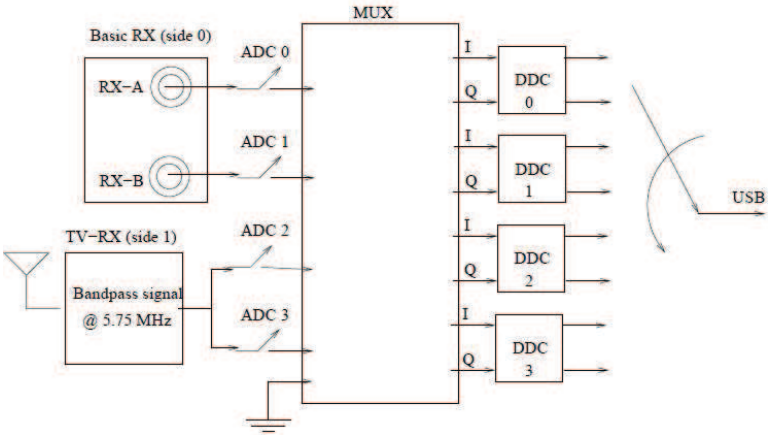

Figure 3.3: Block diagram of USRP receive path [14].

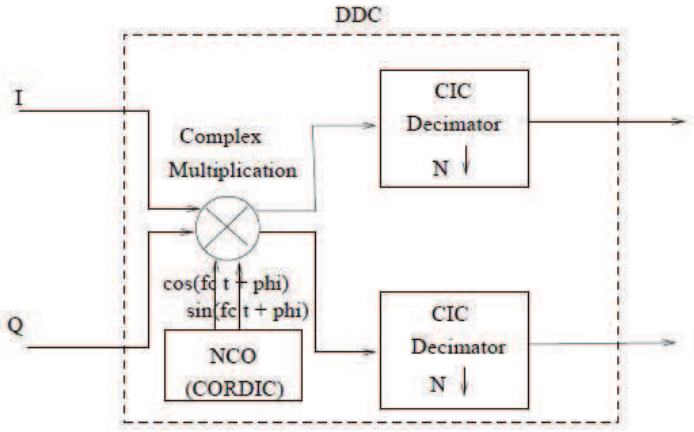

Figure 3.4: Schematic of DDC [14].

The multiplexer (MUX) is like a router or a circuit switcher. It determines which ADC is connected to each DDC input. The MUX can be controlled using the *usrp.set_mux*() method in python. When there are multiple channels (up to four), the channels are interleaved. For example, with four

channels, the sequence sent over the USB would be I0 Q0 I1 Q1 I2 Q2 I3 Q3 I0 Q0 I1 Q1 etc. The only consideration is that the combined data rate on the bus must be 32 Mb/s or less [14].

3.2.2 Software overview of GNU radio

Once the signals get into the computer via USB they are processed by the software codes. GNU radio provides a library of signal processing blocks. A radio can be built by creating a graph (as in graph theory) where the vertices are signal processing blocks and the edges represent the data flow between them. The signal processing blocks are implemented in C++. Block attributes include the number of input and output ports they have as well as the type of data that flows through each. Some blocks have only inputs or only outputs, and serve as sinks and sources respectively. The graphs are constructed and run in the scripting language Python. Python plays a key role in GNU radio programming. GNU radio's software is organized using a two-tier structure. The signal processing applications are built using a combination of Python code for high level organization, policy, graphical user interface (GUI) and other non critical performance functions, while the critical signal processing blocks are written in C++.

This structure has some similarity with the open system interconnection (OSI) 7-layer data network model. Lower layers provide service to the higher layers, while higher layers are transparent to the implementation details carried on at lower layers, but necessary interfaces and function calls. In GNU radio, this layer transparency exists in a similar way. From the Python's point of view, what it does is just to select necessary signal sources, sinks and processing blocks, set correct parameters, then connect them to form a complete application. All the sources, sinks and blocks are implemented as classes in C++. The parameter setting and connecting operations correspond to some sophisticated functions or class methods in C++. However, Python can't see how sedulously C++ has been working. Hence a lengthy, complicated and powerful C++ code is nothing but an interface to Python [14].

3.3 MARIACHI setup - Technical overview

The signal's path from reception to being stored in data files can be broadly classified in three stages as follows:

- Analog front end processing
- USRP mother board processing
- Software processing

The first step is the reception by the antenna tuned to the 67.25 MHz frequency. The signal is transfered using the Quad shielded RG6 cable (Belden 7916A) and waterproof Type F connectors (SPL-6-RTQ). The cables and the connectors are chosen to match the 75 Ω impedance specification of the preamplifier and the TVRX. The impedance matching reduces the cable losses and the preamplifier improves the signal quality (approximately by 10 dB). The preamplifier used in MARIACHI is Wineguard AP 3700 [21]. The frequency response of the pre-amplifier is as shown in Figure 3.5.

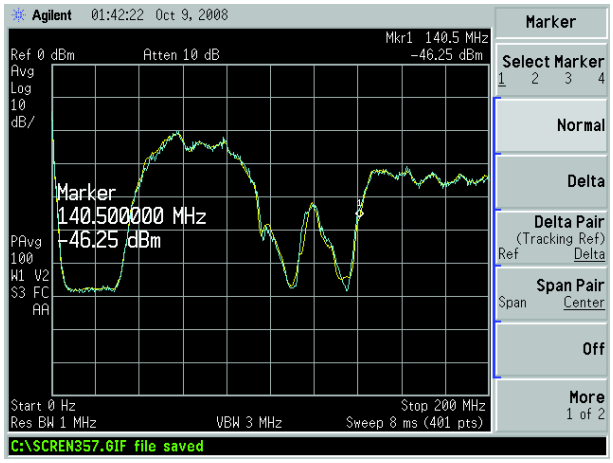

Figure 3.5: Frequency response of Wineguard AP 3700 VHF only pre-amplifier.

After the preamplifier stage, the signal is fed to the two TVRX daughter boards of the USRP. The TVRX boards down-convert and band pass the signal to be processed by the ADCs. After the A/D conversion the signal is decimated using the FPGA and then interleaved for USB transfer. All

these processes are explained comprehensively in later sections. After the USRP processing is complete the data are transfered to the PC using USB. Now the GNU Radio software gets the control of the data and further signal processing steps are executed. Finally the data are stored in data files. The block diagram of the setup is shown in Figure 3.6. The following sections present the mathematical analysis of the signal processing involved.

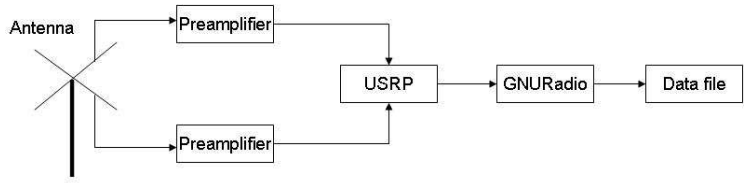

Figure 3.6: Block schematic of recording setup used by MARIACHI.

3.3.1 Analog front end

The RF signal of interest is located in the portion of the spectrum dedicated to TV channel 4 by FCC. The channel is allocated between 66 MHz to 72MHz on the spectrum. The signals used for meteor detection are around the video carrier frequencies of 67.25 MHz and 67.26 MHz. The local station (WNBC-TV New York) has its video carrier at 67.25 MHz. The distant carrier signal is transmitted at 67.26 MHz, and the station is located at Chapel Hill, North Carolina. The frequency shifting effects of the various processing blocks will be illustrated using a spectrum similar to the one shown in Figure 3.7 [22]. Since the signal processing performed by both the daughter boards is identical, we will consider detailed mathematical analysis of one daughter board.

The analog front end of the GNURadio system can be considered as the antenna, cabling, and the TVRX receiver daughter boards. We denote the signal received at the antenna as $r_1(t)$, i.e,

$$r_1(t) = \cos(2\pi f t + \phi) \tag{3.1}$$

The signal is input to the front end of the Microtune tuner module on the TVRX receiver, which contains a high-side mixer, and has an IF mixer output frequency of 44 MHz. We are tuning the system to a frequency of 67.25 MHz,

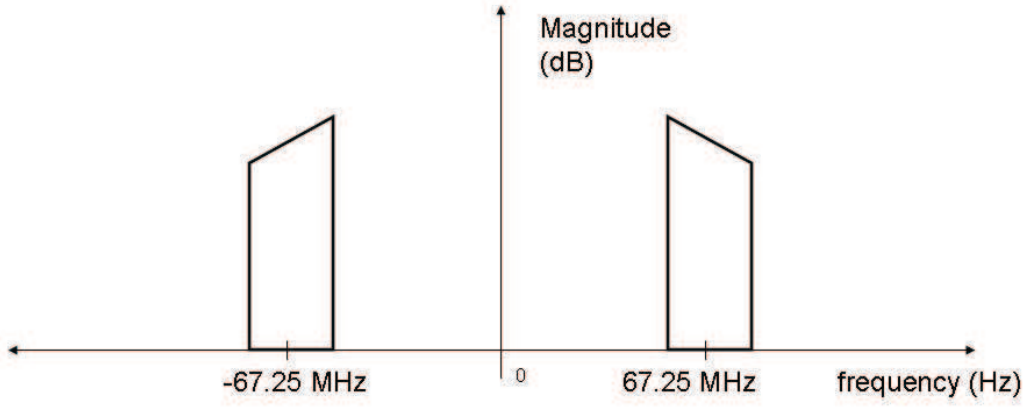

Figure 3.7: RF Spectrum.

so the local oscillator frequency is f_{lo} = 44 MHz + 67.25 MHz = 111.25 MHz. The output of the IF mixer can be represented as

$$g_1(t) = \cos(2\pi f_{lo} t) r_1(t) \tag{3.2}$$

where $r_1(t)$ (from equation 3.1) is the signal received from the dipole of the antenna, f_{lo} is the local oscillator frequency. The output of the mixer is then bandpass filtered with a passband of approximately 40 MHz to 48 MHz. Note that the IF mixer configuration results in a spectral inversion of the signal, that is, an RF signal component at 67.25 MHz + δ will appear at a frequency of 44 MHz - δ. At this point in processing, the first spectral inversion takes place. The resulting spectrum is shown in Figure 3.8. The output of the bandpass filter can be represented as

$$x_1(t) = g_1(t) * h_1(t) \tag{3.3}$$

where, $h_1(t)$ is the impulse response of the bandpass filter and $g_1(t)$ (from equation 3.2) is the output of the mixer.

This signal is output from the Microtune module as an analog differential signal. The differential pair is then connected from the TVRX daughter board to the USRP mother board, where it is fed to the differential inputs of the ADC. Only one differential input of the AD9862 processor is fed using the output of the tuner module. Since the AD9862 expects an in-phase and quadrature input if the sampling is complex, in this case only real samples are fed hence the second input is left unconnected.

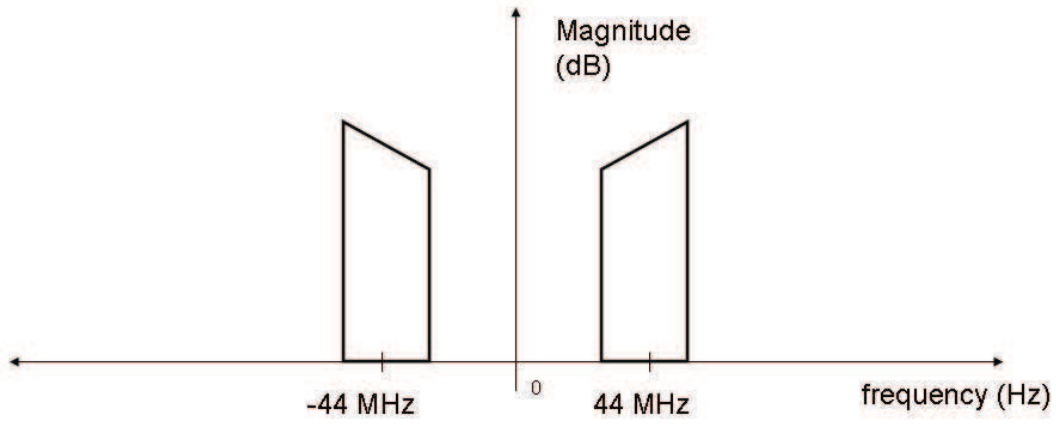

Figure 3.8: Mixer output.

3.3.2 USRP mother board processing

The A/D converter on the USRP board samples at a rate 64 MS/s. The output of the bandpass filter from the daughter board is fed to the ADC on the mother board. The sampled signal can be represented as

$$y_1(n) = x_1(t) \sum_{n=-\infty}^{\infty} \delta\left(t - \frac{n}{f_s}\right) \tag{3.4}$$

where, f_s is the sampling frequency of the USRP ADC and $x_1(t)$ (from 3.3) is the output of the daughter board. The stages involved in USRP processing are shown in Figure 3.9. The functional schematic of the USRP is shown in Figure 3.10. As it can be seen from Figure 3.9 the output of the daughter board is fed to both ADCs.

Thus, an RF signal component originally at a frequency of 67.25 MHz + δ will appear at 44 MHz - δ after the band pass filtering. When this band pass filtered signal centered at 44 MHz is sampled at 64 MS/s aliasing will occur and the original signal will occur at 20 MHz + δ. And at this stage the second spectral inversion takes place. Hence the initial inversion resulting from mixer used in daughter board gets reversed and the original shape of the spectrum is restored. The sampled spectrum is as shown in Figure 3.11.

The first digital processing block of the USRP is the digital down converter (DDC). This block multiplies the real input signal by a complex exponential to shift the tuned frequency to DC. In this case, it means

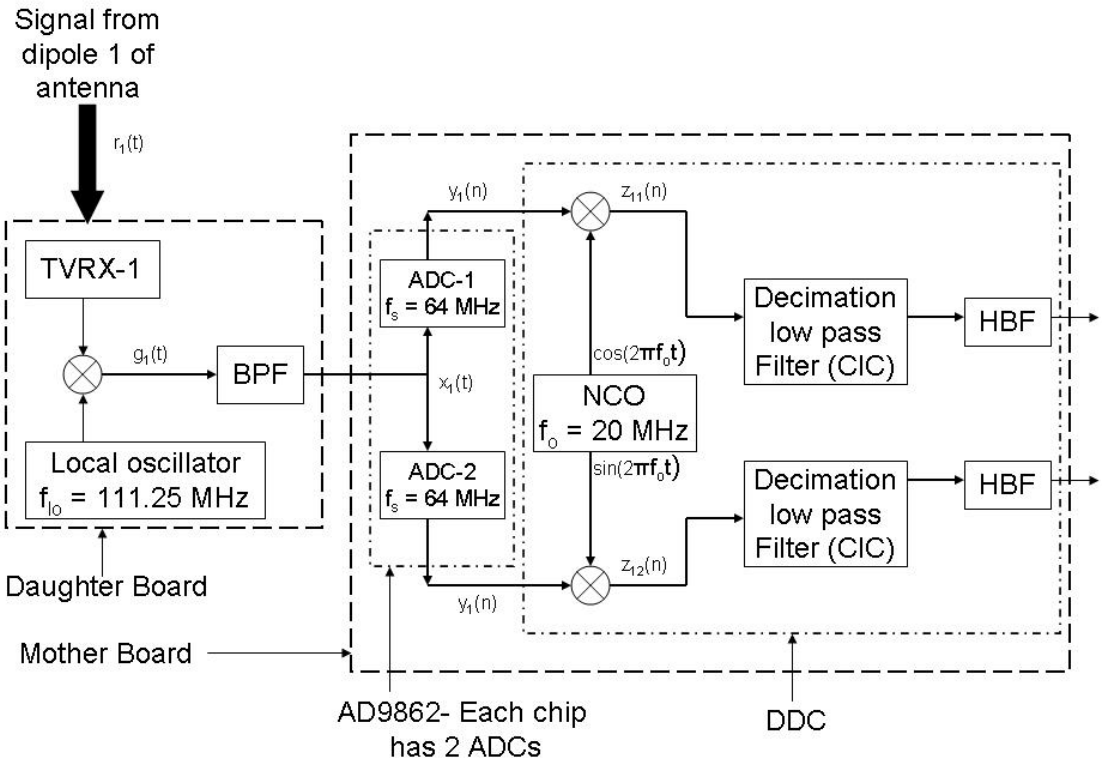

Figure 3.9: Block diagram of USRP stages.

multiplying the signal from (3.4) by $\exp^{-j2\pi f_o t}$, where $f_o = 20$ MHz, which

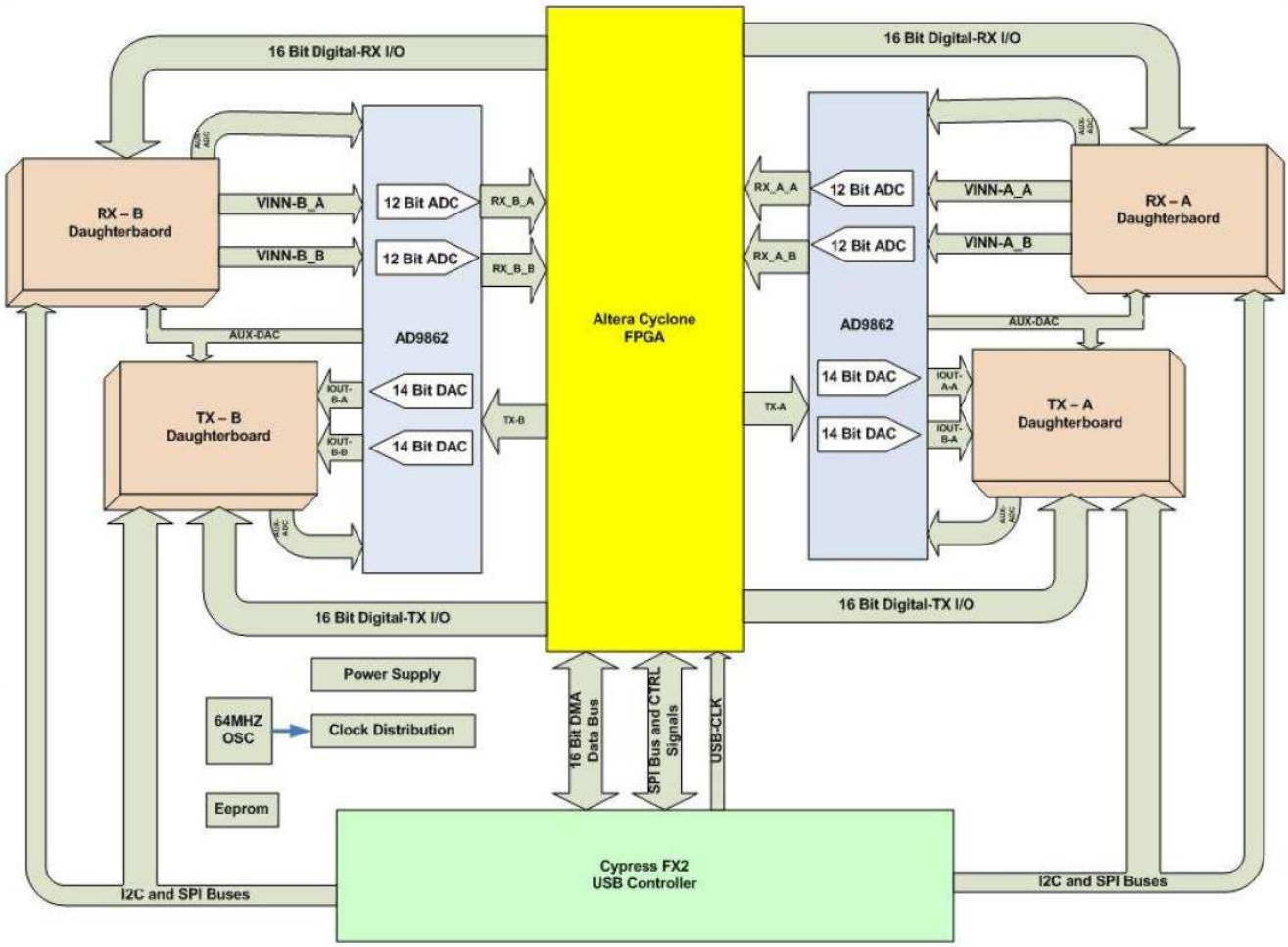

Figure 3.10: Functional schematic of the USRP board [14].

gives us

$$\begin{aligned} z_{ddc}(n) &= y_1(n)\exp^{-j2\pi f_o n} \\ &= x_1(t)\sum_{n=-\infty}^{\infty}\delta\left(t-\frac{n}{f_s}\right)\exp^{-j2\pi f_o n} \\ &= (g_1(t)*h_1(t))\sum_{n=-\infty}^{\infty}\delta\left(t-\frac{n}{f_s}\right)\exp^{-j2\pi f_o n} \end{aligned} \tag{3.5}$$

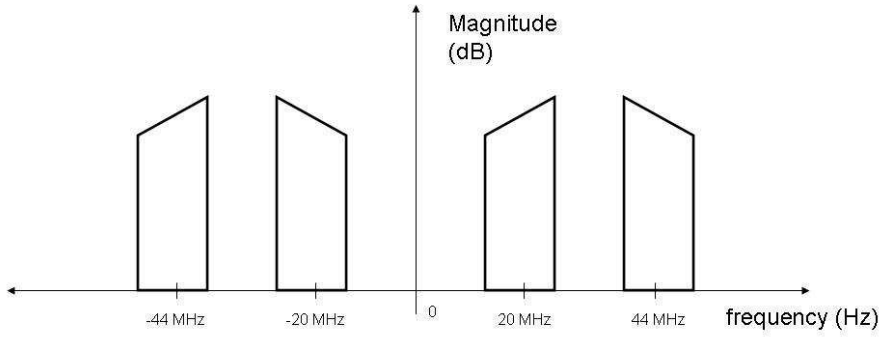

Figure 3.11: Sampled spectrum.

The following equation is obtained by using equations (3.1), (3.2), (3.3), (3.4) and (3.5)

$$z_{ddc}(n) = ((r_1(t)\cos(2\pi f_{lo}t) * h_1(t)) \sum_{n=-\infty}^{\infty} \delta\left(t - \frac{n}{f_s}\right) \exp^{-j2\pi f_o n} \tag{3.6}$$

Let, $z_{ddc}(n) = z_{11}(n) + jz_{12}(n)$, where $z_{11}(n)$ and $z_{12}(n)$ represent in-phase and quadrature components or

$$\begin{aligned} z_{11}(n) &= r_1(t)\cos(2\pi f_{lo}t) \sum_{n=-\infty}^{\infty} \delta\left(t - \frac{n}{f_s}\right) \cos(2\pi f_o n) \\ z_{12}(n) &= -r_1(t)\cos(2\pi f_{lo}t) \sum_{n=-\infty}^{\infty} \delta\left(t - \frac{n}{f_s}\right) \sin(2\pi f_o n) \end{aligned} \tag{3.7}$$

After this stage, a component of the RF signal at frequency of 67.25 MHz will appear at DC in the complex digital representation. The component originally at 67.25 MHz + δ will appear at $f = \delta$, and components originally at 67.25 MHz - δ will appear at $f = -\delta$. Given that the RF signal components at $f_c + \delta$ and $f_c - \delta$ are not necessarily related to each other, the complex signal representation is natural for these types of signals. The spectrum of the output after the DDC is as shown in Figure 3.12.

At this point, the signal is filtered and decimated using a Cascaded Integrator Comb (CIC) filter. This filter has a response given by

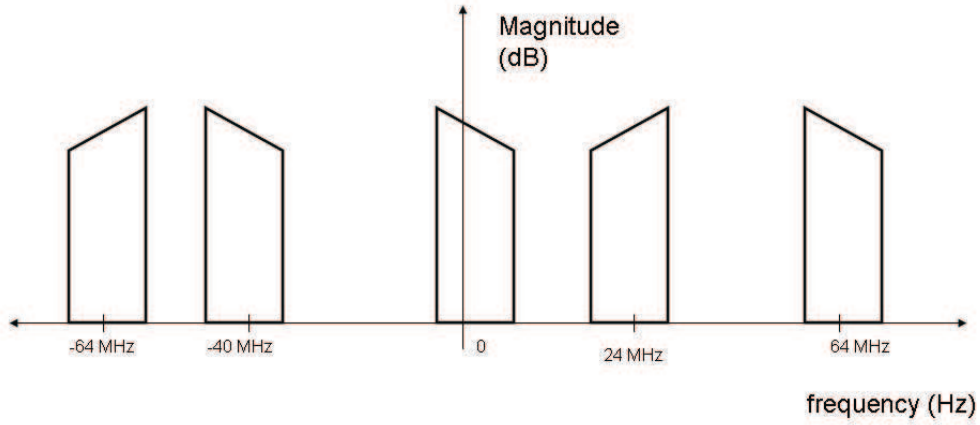

Figure 3.12: Complex spectrum at the output of the DDC.

$$H(z) = \left(\frac{1 - z^{-D}}{1 - z^{-1}}\right)^{M} \tag{3.8}$$

where D is the decimation rate and M is the number of cascaded sections. In our implementation $D = 8$ and $M = 4$. Figure 3.13 shows the frequency response of the CIC filter. The CIC filter structure is very simple to implement in hardware, which justifies its use in USRP boards, even though it doesn't have the most desirable frequency response characteristics [23]. The CIC needs two inputs to generate the in-phase (I) and quadrature (Q) components. The same stream of data is multiplied by sine and cosine to generate the I and Q components for the CIC filters. The coordinate rotation digital computer (CORDIC) algorithm [24] is used to generate the two components for the CIC inputs. The Numerically Controlled Oscillator (NCO) generates the fixed frequency signal needed for shifting the spectrum to DC. The scheme is shown if Figure 3.14. The output of the two CIC filters can be represented as

$$\begin{aligned} z_{11CIC}(n) &= z_{11}(n) * h_{CIC}(n) \\ z_{12CIC}(n) &= z_{12}(n) * h_{CIC}(n) \end{aligned} \tag{3.9}$$

where, $h_{CIC}(n)$ is the impulse response of the CIC decimation low pass filter.

The final processing step in the USRP FPGA is the half band low-pass filtering and decimation by a factor of 2. The frequency response of the half-

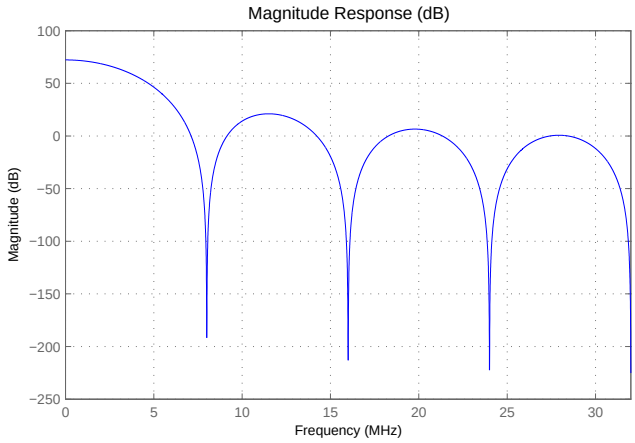

Figure 3.13: Magnitude response of the CIC filter.

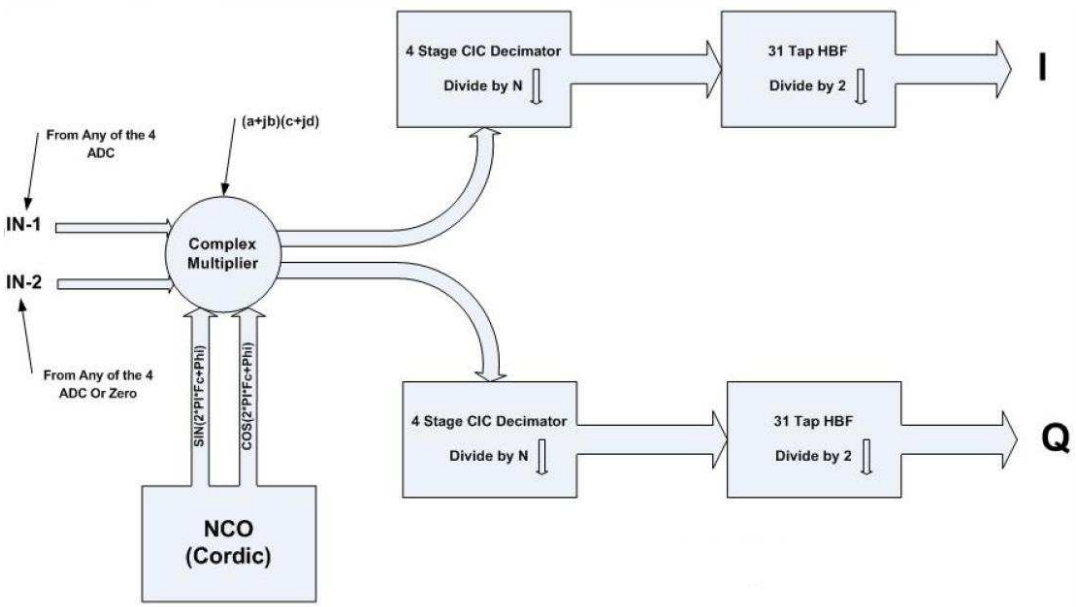

Figure 3.14: Block schematic of DDC [14].

band filter is shown in Figure 3.15. The output of the half band filter can be represented as

$$\begin{aligned} z_{11f}(n) &= z_{11CIC}(n) * h_{HBF}(n) \\ z_{12f}(n) &= z_{12CIC}(n) * h_{HBF}(n) \end{aligned} \tag{3.10}$$

where $h_{HBF}(n)$ is the impulse response of the half band filter with $f_s = 8$ MHz.

After the half band filter, the data are transmitted to a PC over a USB interface. Hence the final data rate becomes 4 MS/s per daughter board. Thus, the final output of processing for the TVRX-1 daughter board samples can be represented as

$$z_{1f}(n) = z_{11f}(n) + jz_{12f}(n) \tag{3.11}$$

where z_{11f} and z_{12f} are the filtered in-phase and quadrature components, respectively.

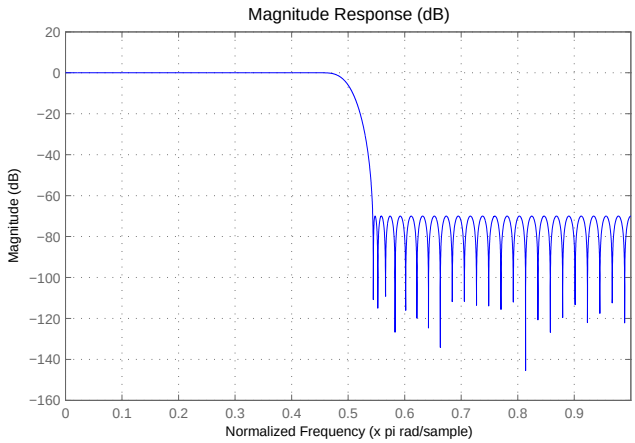

Figure 3.15: Magnitude response of the half-band filter.

3.3.3 Software processing

When the data are received on the PC it is again low-pass filtered with a cutoff frequency of 250 kHz. The data are then decimated (by a factor of 8 in the current case) to a sampling rate of 500 kHz. The frequency response for

the entire bandwidth is shown in Figure 3.16. The passband and transition bands are shown in Figure 3.17.

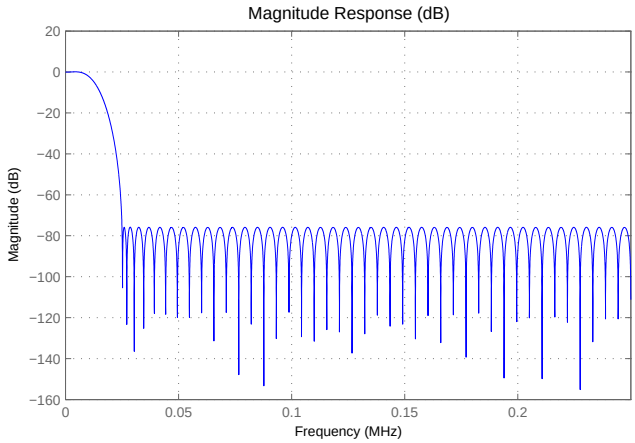

Figure 3.16: Magnitude response of the first PC filter.

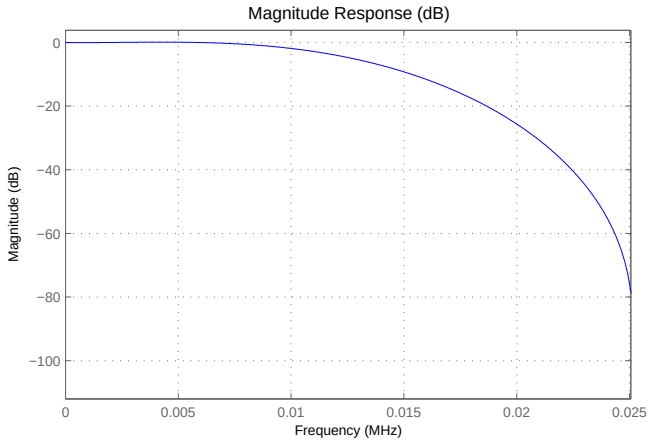

Figure 3.17: Magnitude response of the first PC filter (passband).

The next stage is a phase-locked loop (PLL) that corrects for the frequency offset and drift of the local oscillator in the TVRX receiver. This is done by tracking the local video carrier, based on the assumption that it will always be the strongest signal in the range 67.25 $\pm$ 2 kHz (if some other signal in the range is stronger than the local carrier, the PLL may lock

to this other signal instead). The PLL estimates the instantaneous phase and frequency of the carrier and corrects the signal based on the estimated values. The output of this stage is

$$g_{pll}(t) = g(t)\exp^{-j\left(2\pi\widehat{f}(t)t+\widehat{\phi}(t)\right)} \tag{3.12}$$

where $\widehat{f}(t)$ and $\widehat{\phi}(t)$ are the estimated instantaneous frequency and phase, respectively.

The final processing stage is another low-pass filter. This filter has a passband below 25 kHz and a cutoff frequency of 35 kHz. The data are then decimated to a sampling rate of 100 kHz. The frequency response of this filter for the entire bandwidth is shown in Figure 3.19. The passband and transition band are displayed in Figure 3.20. After this stage, the complex data is written to a file.

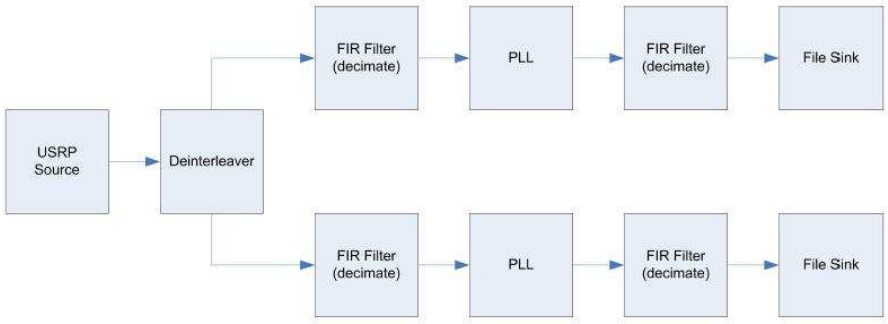

Figure 3.18: Functional schematic of the PC processing.

3.4 Challenges

Changing oscillator frequency

The local oscillators used on the TVRX daughter boards have a frequency drift and a constant offset. Both the parameters are completely different for every single daughter board. The unstable frequency can be a problem during

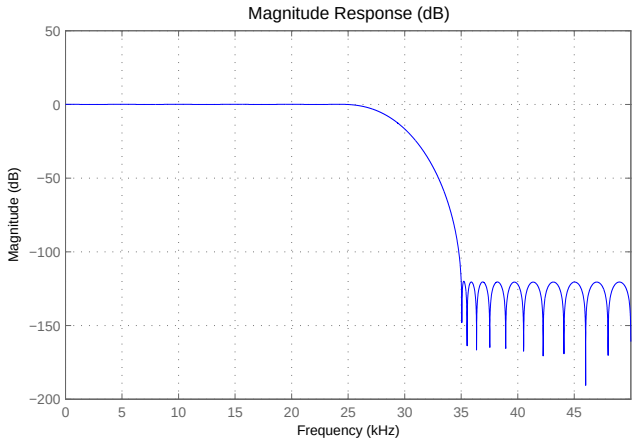

Figure 3.19: Magnitude response of the second PC filter.

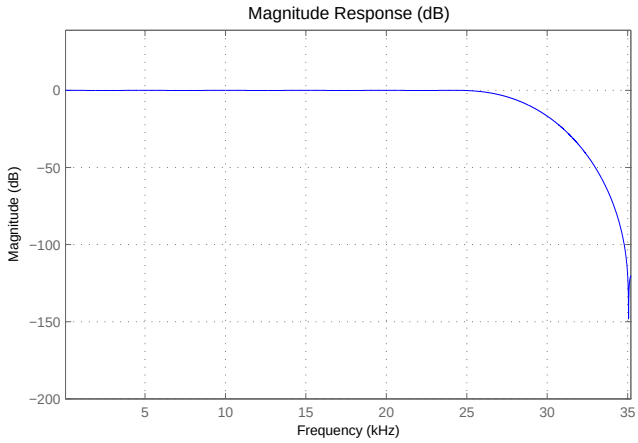

Figure 3.20: Magnitude response of second PC filter (passband).

detection. The down conversion is severely affected since the intermediate frequency gets affected by this instability.

One possible reason for oscillator drift is sudden turning on of the device. From Figure 3.21 it can be seen that there is a very drastic drift during the first 300 s after the operation starts. Later the drift is comparatively reduced to a few Hertz. The setup setting used for test are

- Input Signal: Signal generator at 67.26 MHz (Sine wave).

- Radio Setting: 3.2 kHz Bandwidth
- Recording Frequency: 67.259 MHz

Hence for the above setup the output should be 1 kHz but the TVRX errors add an offset of almost 1.8 kHz with a constant fluctuation. The distribution of output frequency is shown in Figure 3.22

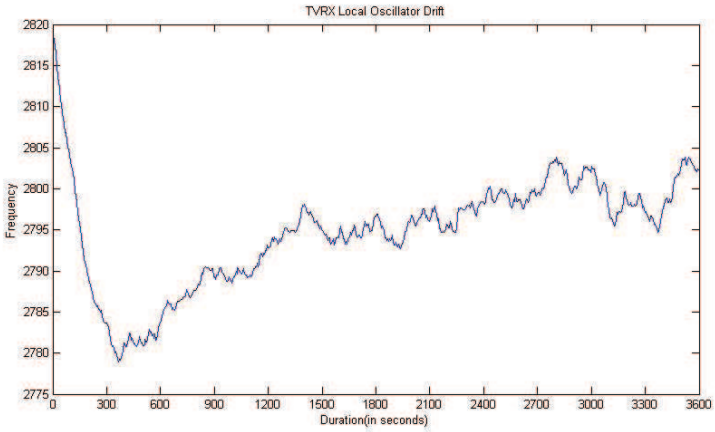

Figure 3.21: TVRX Local oscillator drift.

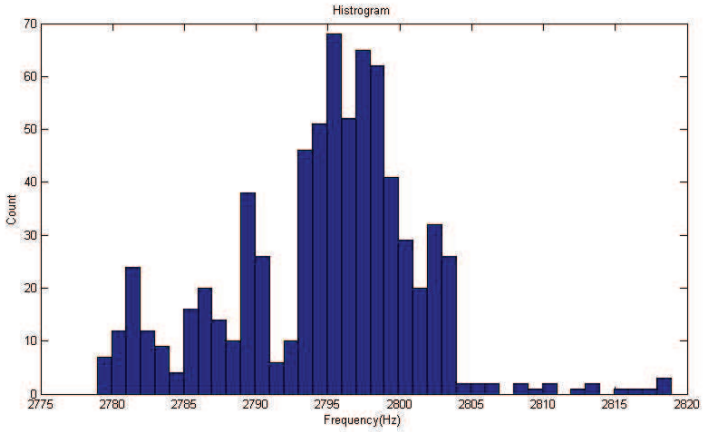

Figure 3.22: Histogram of the center frequency value.

The solution currently implemented is a software PLL. The PLL is coded in Python. The PLL locks to a stable local TV station video carrier frequency of 67.25 MHz. Since the wide band operation of GNU radio allows this

Gain control

The gain of the radio is set using the software code. But the actual translation of the input settings to hardware does not happen. For example reducing the gain by 10% results in different values when used at 90% and 50%. Hence the software gain settings at all the recording radios should be kept consistent to ensure integrity of data.

Filter performance

In the case of GNU radio the filters are implemented in software. The performance of the software can be optimized by a better approach while coding. To save some time of execution, coefficients for filters are generated using MATLAB and uploaded at runtime from a file, which reduces the filter creation time.

ADC saturation

Due to recording at a very high bandwidth signal there is always a risk of ADC getting saturated. In MARIACHI the recording large part of channel 3 and 4 causes the ADC to saturate. This problem is solved by adjusting the gain.

Data processing

Online processing of data is very difficult due to large amounts of data being recorded. The average amount of data currently recorded for a bandwidth of 100 kHz is approximately 5.76 GB per hour. Processing requires lot a of computation power and increases the cost of setup considerably.

Currently the most stable detection algorithm is able to compress results to 18 MB files for 1 hour of data, that is 9 MB per dipole antenna. But this method will be modified depending on the progress of event feature extraction procedures.

Chapter 4

Signal processing

4.1 Introduction

The motivation behind building this DAQ system is the detection of meteors that create ionized trails in the ionosphere. The detection is implemented by several steps of signal processing. In particular, the aims of signal processing are:

- Detection of potential candidates for reflected signals,
- Estimation of the parameters of the candidate signals,
- Processing of the candidates and their classification based on the estimated parameters (a detected signal may represent a local interference or a reflected signal).

These problems are interrelated. For example, the classification and the location of the reflector are based on some estimated parameters of the reflected signal.

The problem of detection of forwardly scattered signals can be rather challenging for several reasons. One is that the signals that have to be detected are random and may be rather weak and the other is that the detection is to be carried out in the presence of many local signals that can occur in the monitored frequency bandwidths. The bandwidths have to be carefully selected so that they are wide enough to allow detection of events of short duration.

4.2 Detection and classification of events

4.2.1 Detection

The cross dipole basically allows acquisition of two signals. The detection exploits the polarization of the signals, i.e., the orientation of their electric fields. The received signals often do not take on their transmitted polarization because of the depolarization mechanism [25]. The polarization of the signals sent by the transmitters vary from one transmitter to another and they are either horizontal or vertical [26]. In the case of the MARIACHI setup, TV stations transmit with horizontal polarization.

Let the recorded signals after filtering, downshifting and sampling be denoted by x_t and y_t, where t represents a discrete time index, and x and y are the signals captured by two dipole antennas. In general, there are two hypotheses: the null hypothesis is that data do not contain a reflected signal and the alternative hypothesis is that they do. They can be expressed as

$$\begin{aligned} \mathcal{H}_0 \quad : \quad & x_t = a_x z_t + u_t \\ & y_t = a_y z_t + v_t \end{aligned} \tag{4.1}$$

$$\begin{aligned} \mathcal{H}_1 \quad : \quad & x_t = a_x z_t + b_x s_t + u_t \\ & y_t = a_y z_t + b_y s_t + v_t \end{aligned} \tag{4.2}$$

where z_t is a local signal which is always present due to line of sight reception, s_t is a signal that has undergone reflection, and u_t and v_t are noises. The coefficients a_x and a_y are defined by the polarization of the emitted signals and by the receiving antennas, a_y and b_y are similarly defined by the polarization of the emitted signals and by the receiving antennas but also by the physics of the reflection. All these constants are unknown. The signals z_t and s_t are independent, zero mean and non stationary, and their powers vary with time. We assume that the noises u_t and v_t are zero mean and stationary and that their powers remain constant during the short intervals over which we compute the powers of x_t and y_t. We do not assume anything, however, about the distribution of the noises. We note here that the model given by equations (4.1) and (4.2) can be expressed with a more detailed set of equations that involve the concept of array manifold [27]. However in this case it is not necessary.

The first step to detection is to simply compute the powers of x_n and y_n by

$$P_{x,t} = \frac{1}{N} \sum_{t=-\frac{N}{2}}^{\frac{N}{2}} x_t^2 \quad ; \quad P_{y,t} = \frac{1}{N} \sum_{t=-\frac{N}{2}}^{\frac{N}{2}} y_t^2 \tag{4.3}$$

where it is assumed that the interval contains $N+1$ samples, and N is an even number.

The next step is to compute the ratio of the powers,

$$\rho_t = \frac{P_{y,t}}{P_{x,t}} \tag{4.4}$$

The ratio ρ_n will have different distributions under the two hypotheses. A standard approach for detecting the signal is selecting hypothesis $\mathcal{H}_1$ based on the Neyman-Pearson test would be to identify the distribution of ρ_n under $\mathcal{H}_0$ and then determine the thresholds that would provide a predefined false alarm rate [28]. This approach is not considered in this work, as it will be published independently in near future.

4.2.2 Classification of events

There may be reflections that are detected but are not a result from meteor trails. The detection process separates reflections due to meteors from those from aircrafts, lightning discharges, sporadic E skip, tropospheric bending, F2 skip, auroras, and trans equatorial scatter. Different signals leave their signatures on the received signals, which allow for their classification. The classification can be done by first determining the features of the various types of detected signals and based on them building classifiers [29]. Features that are usually employed for classification are signal duration, strength, spectral contents and Doppler shifts. Classification of signal requires processing of the data in the time domain, the frequency domain and time-frequency domains. The algorithm is presented in the next section.

4.2.3 Detection algorithm

Winradio file processing

- The input to the algorithm is filtered and down sampled data.

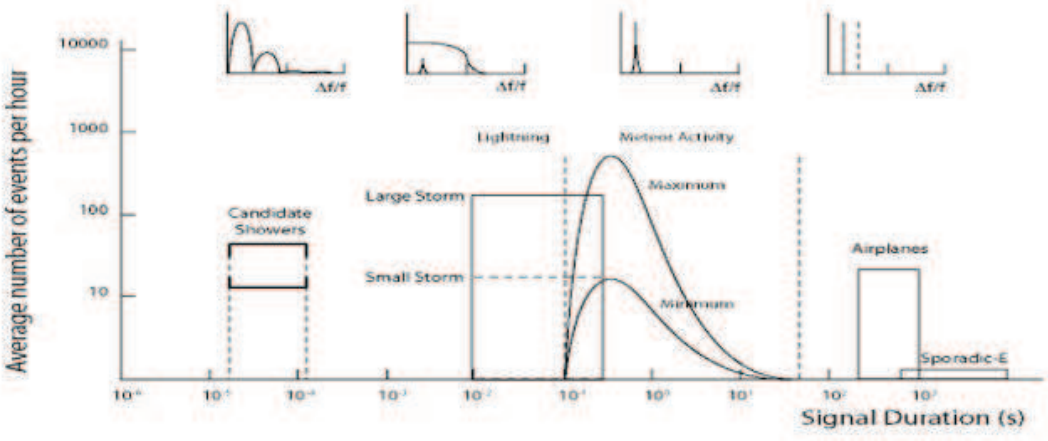

Figure 4.1: Event durations and approximate hourly frequency.

- The duration of meteor events is always greater than 0.1 s. Taking advantage of this fact, the data are considered as collection of bins of 0.1 s instead of individual points.
- The power of all the bins is calculated. Average noise power is computed over 60 mins. This noise power is used for signal to noise ratio (SNR) calculations.
- SNR of all the bins is calculated . Every bin with SNR above 20 dB is given a weight of 1 and the rest are given a weigth of 0.
- From the weighted data the runs of 1s are counted to find the length of events.
- All events between 0.1 s to 60 s get classified as candidate events on each channel. Details of few non meteor events and corresponding durations are shown in Figure 4.1.
- Now the ratio powers of two channels from these selected bins is taken. All the events with ratio greater than 5 are possible meteors.

GNU Radio data processing

- The output of the data acquisition module are two binary files. Each file corresponds to one of the antenna dipoles. The files are written at

a rate of 100 KS/s. The content of these files is complex spectrum of ±25 kHz centered at 67.25 MHz.

- The first step here is to filter out bands of interest and write them to separate files. To accomplish this task we use filter modules from the GNU Radio modules. Bands of ± 500 Hz are extracted and decimated before being written to files. For example, possible frequencies of interest are, the local carrier, 8 - 12 kHz offsets, 15.75 kHz offset (raster scan frequency). The idea is shown in Figure 4.2.

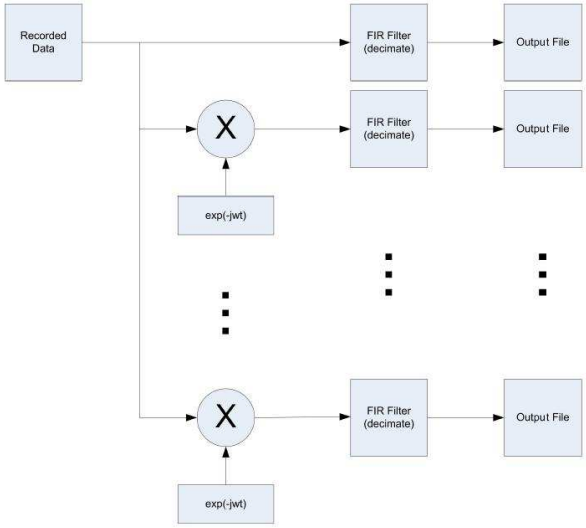

Figure 4.2: The process of offset creation.

- Now each file is read using Matlab or Octave. Even after decimation, the files are too big to be read at once. Hence, the data are treated as segments of 0.05 s at a time.

- The data vectors of 0.05 segments are used to calculate the coherency matrices. These coherency values are then written to files for further processing.

- For classification of events, two primary criteria are used. First, the average energy of a segment at 10 kHz should be at least 1.5 times the

average energy during that entire hour. Second, the phase of the carrier should be greater than $\pm\frac{\pi}{10}$. This value of phase angle is deduced from the experimental data. In the future this value will be corrected.

- Finally once the candidate events are found they are classified depending on their durations.

4.3 Synchronization

Synchronization of the data from all recording stations is essential to ensure the integrity of data collected by the entire system. For localization the synchronization between all the receiving stations is the most important thing. As the sampling rate increases, the accuracy of time stamping of data has to increase. The need of a specialized mechanism arises because the computer clocks are not very accurate. The accuracy needed to detect UHECR is of the order of microseconds but the computer clocks are accurate within a few seconds only.

Ideally if all sites are synchronized, the data can be correlated sample to sample precisely. It is impossible to have a time tag for every sample hence the closest solution is have self reference time markers embedded in the data. One possible solution is to use a global position system (GPS) disciplined timing signal generators and frequency reference as the source of time at every receiver station. The following section explains the synchronization scheme proposed for the MARIACHI DAQ system.

4.3.1 Synchronization scheme

The ultimate goal of this scheme is to make sure that data from all receivers can be aligned with an accuracy of few microseconds. One way of doing this is to embed the time markers in the data before it gets fed to the GNU Radio. The setup to be implemented is shown in Figure 4.3.

The RF switch is used to blank the signal at a fixed period starting at a fixed time. For example all stations start recording the data at 1 PM according to their system clocks. We assume that all the computers are synchronized with network clocks via the Internet ensuring only a time skew of few seconds among them. The GPS instrument starts generating pulses at a frequency of pulse every 10 minutes. With pulse trigger from the GPS the

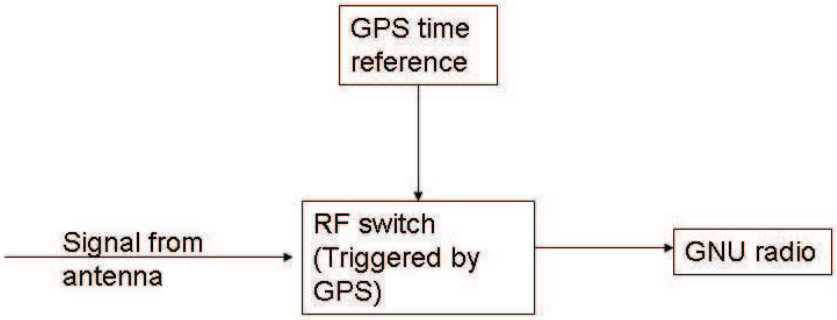

Figure 4.3: Setup for proposed synchronization scheme.

radio switch will turn off and blank the signal for the pulse duration. When the hourly data from all stations get collected on the server these blanks can be aligned and the data can be synchronized. Figure 4.4 shows how the data will look after the scheme is implemented. Some of the delays which cannot be avoided and approximated are

- Computer system clock delay.
- Delay between the execute command to run the script and actual beginning of the execution on hardware.
- Delay between the file creation and writing the data to the file after processing (commonly referred as I/O delays).

With these delays the data between two stations will always be out of sync by a few seconds in the worst case. But comparing the duration between two time markers this is very small and hence the markers at the beginning of the hour can be safely used for aligning the data.

In the MARIACHI setup, Spectrum instruments Intelligent time reference TM4 [30] GPS instrument is used to generated the pulses. The GPS device has a function to generate programmed output pulse (POP). The GPS device is connected to a computer via a serial port. Figure 4.5 shows the back panel of TM4 and Figure 4.6 shows the pin configuration of the serial connector. The POP output is at pin 12.

The TM4 has a user interface which allows the user to program the pulse duration, polarity, period and time to start generating the pulses. The interface for POP of TM4 is shown in Figure 4.7.

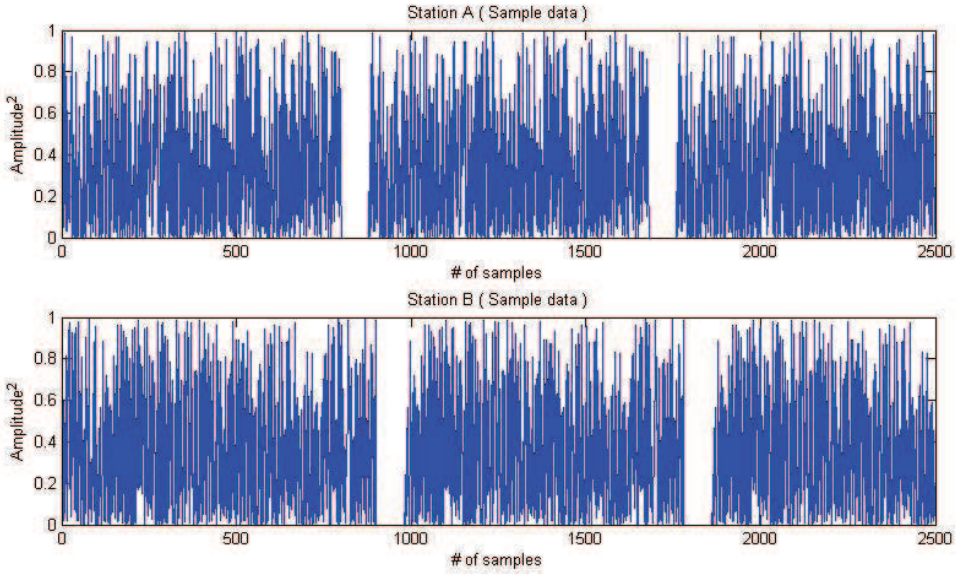

Figure 4.4: Sample data streams of 2 stations.

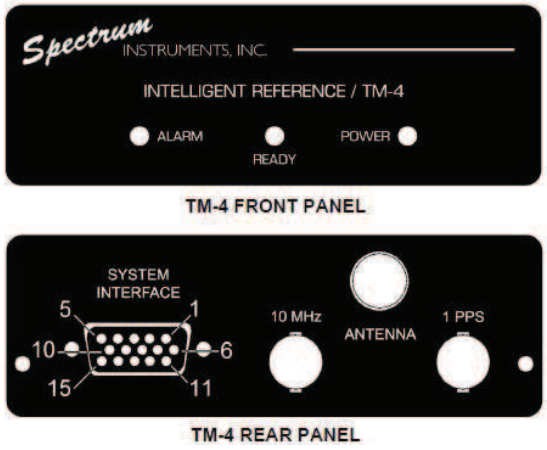

Figure 4.5: TM4 GPS panels.

4.4 Localization

Localization is the final step of the process. After the detection is completed at all the individual stations, the source of reflection has to be localized and

PIN	SIGNAL NAME	FUNCTION
1	OUT2	10 MHZ TTL OUTPUT or CUSTOM OUT
2	GND	SIGNAL/POWER GROUND
3	CPTXD232	RS-232 SERIAL DATA TO HOST
4	CPRXD232	RS-232 SERIAL DATA FROM HOST
5	PPS/AUX232	PPS/CUSTOM – SEE DESCRIPTION
6	TPTXD232	TIME PORT RS232 OUTPUT
7	MUXOUT1A	MULTIPLEXER 1, A OUTPUT
8	ALM	ALARM OUTPUT
9	GND	SIGNAL/POWER GROUND
10	EVENT	EVENT INPUT
11	DCIN	POWER IN (9-35 VDC)
12	POP	PROGRAMMED OUTPUT PULSE
13	MUXOUT2	MULTIPLEXER 2 OUTPUT
14	IN1	RESERVED – SEE DESCRIPTION
15	OUT1/IRIG/IN2	OUTPUT/TIME CODE/CUSTOM INPUT

Figure 4.6: Pin description of serial port interface of TM4.

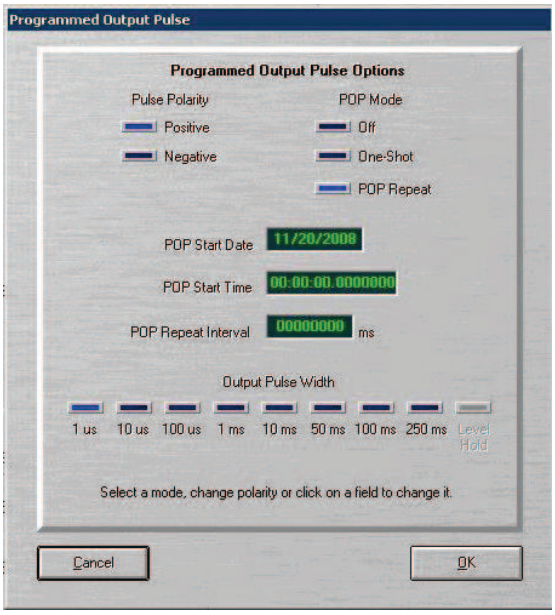

Figure 4.7: Programmed output pulse menu of TM4 user interface.

the direction of arrival can be estimated. One approach to find the position of the reflector can be based on the received signal strength [31]. Another way is to exploit polarization diversity (for instance, in [32], a linear array of crossed-dipoles is used to estimate the angle of arrival and polarization of coherent

signals). Yet, other approaches might include use of time of detection of the reflected signal, which requires a very careful synchronization of the stations. A method that combines all the previously mentioned approaches is also possible.

4.4.1 Signal power - based method

A mathematical model that describes the received signal power from one emitter by the receiver antenna is given by

$$P_i(t) = \frac{K(t)}{||\mathbf{r} - \mathbf{l}_i||^2} + e_i \tag{4.5}$$

where $P_i(t)$ is the received power at the i-th station at time t, $\mathbf{r}$ is a vector that denotes the position of the reflector for which we assume that is stationary, $\mathbf{l}_i$ is the localization of the i-th antenna, $K(t)$ is a parameter that varies with time, it is common for all stations[1] and depends on various parameters including the gains of the crossed-dipoles, the gains of the receivers, and the (varying) transmitted power, $||.||$ stands for Euclidean distance, and e_i is the error in the modeling. It is important to note that $K(t)$ is unknown when the signal is a reflected signal.
The estimation of $\mathbf{r}$ from received powers at five or more stations as described above, amounts to nonlinear optimization. This, in general, can be accomplished by one of existing schemes, such as, the Newton-Raphson scheme [33]. The problem becomes more challenging when there is also a local signal in the measured power. In that case, the model is

$$P_i(t) = \frac{K_l(t)}{||\mathbf{r}_l - \mathbf{l}_i||^2} + \frac{K(t)}{||\mathbf{r} - \mathbf{l}_i||^2} + e_i \tag{4.6}$$

where $K_l(t)$ corresponds to the local signal and $\mathbf{r}_l$ is the localization of the local transmitter, which is assumed known. The optimization can be applied even if there is a local signal in the data. If it is assumed that the power of the local signal does not vary fast with time (not as fast as the appearance of the reflected signal), then the contribution of the local signal can be estimated when the reflected signal is absent (during an interval preceding the appearance of the reflected signal). Subsequently the obtained estimate

[1]The varying parameter $K(t)$ can be made the same for all the stations after careful calibration.

can be subtracted from the total power, which leaves only the reflected signal. The optimization uses the information such as the orientation of the antennas and their radiation patterns.

4.4.2 Time of reflection - based method

If all the data recording stations are precisely synchronized to a margin of less than UHECR event duration, then precise time of reflection can be used for localization of the source. To implement this method at least four receiving stations are required. The basic concept of trilateration is used in this algorithm.

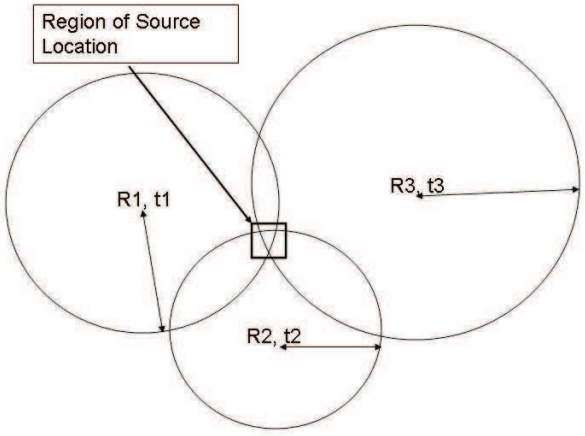

Figure 4.8: Concept of trilateralization in 2-D.

The concept relies on the fact that the reflected signal travels at speed of light. Hence for any given receiver station the source of reflection could be on the surface of a hemisphere with radius equal to the product of the speed of light and the time delay. When such regions from at least four neighboring stations are found, the source can be localized in three dimensions. An example for localization in two dimensions is shown in Figure 4.8.

4.5 Results

This section presents examples of candidate events.

- Figure 4.9 shows a sample of the forward scattered signal. The figure is a 3D representation of the time frequency plot. The figure shows the offsets and the local carrier plotted together in time. The red, blue and black lines represent the 11 kHz, 10 kHz and 9 kHz offsets respectively. The z axis is the ratio of power of the two dipoles. From the figure it can be seen that there is a significant increase in power around the distant transmitter frequency but the local carrier is unaffected.

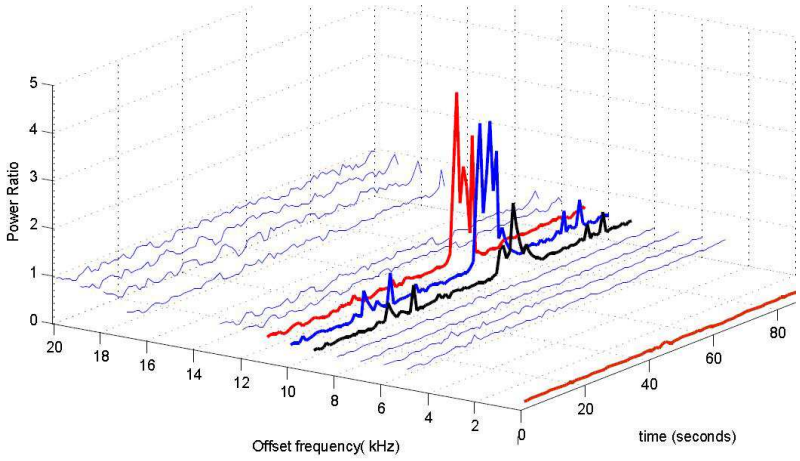

Figure 4.9: Visual illustration of the forward scatter concept (Plot duration: 100 s).

- Candidate event: Figure 4.10 shows a candidate event. The data were recorded with a setting of 2 kHz bandwidth and sampling rate of 96 kS/s. The center frequency was 67.26 MHz. According to the forward scatter theory, the increase in energy at distant transmitter frequency is an indication of reception from the distant transmitter. The amplitude and duration of increase qualify the event as a candidate.

- In Figure 4.11 we show results from data recorded in November, 2008. On the horizontal axis we plotted the time expressed in hours and on the vertical axis the number of events per hour that needed to be processed. The data recording was started at 11/08/2008 00:00:00 UTC and was stopped after 17 days ($17 \times 24 = 408$ hours). To keep the data compact, the minimum resolution of the graph was limited to one hour. It is interesting to point out that the results showed the expected daily

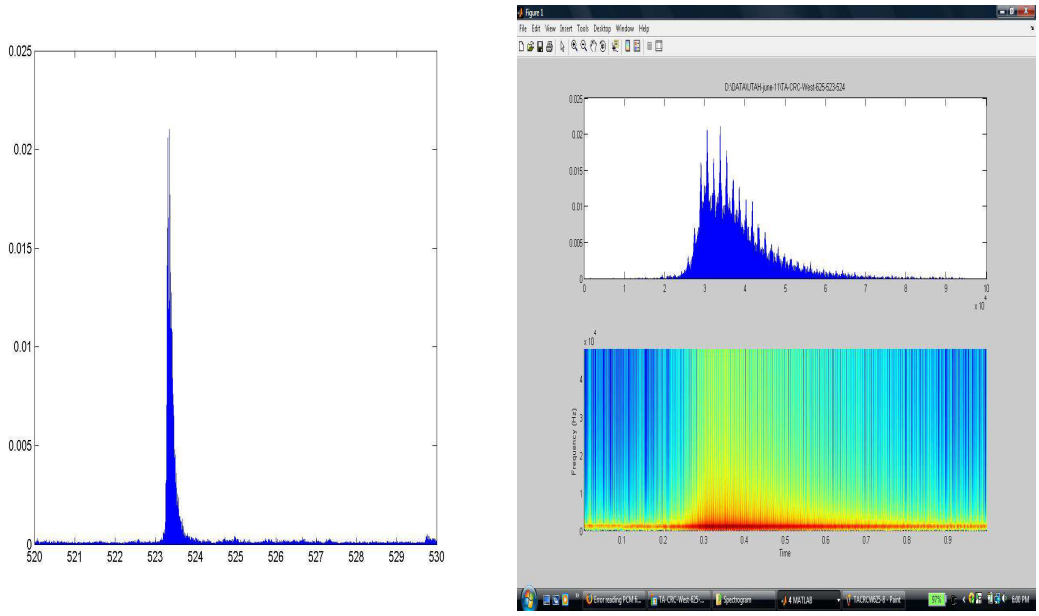

Figure 4.10: A 1 s long candidate event (L) and its corresponding spectrogram (R) (Plot duration: 10 s).

maxima and minima patterns of events according to the local time [4]. Recall that the meteor activity in a day is maximum around 6 AM local time and minimum around 6 PM local time (see results in Figure 4.11). The periodic peak and valley pattern is called Diurnal pattern [7].

- Multiple candidates: Another interesting phenomenon is the occurrence of multiple events in quick succession. During meteor showers such occurrences are normal but under normal circumstances there is a different possibility. It is possible that a huge meteor breaks in fragments and creates multiple trails. But there is no way to identify such trails with certainty.

- Underdense regime: As explained in Chapter 2 the meteors are broad classified in two regimes. Figure 4.13 shows which can be classified as an underdense meteor. The most distinct characteristic if such events is the exponentially decreasing amplitude.

- Overdense regime: Figure 4.14 shows a possible overdense meteor

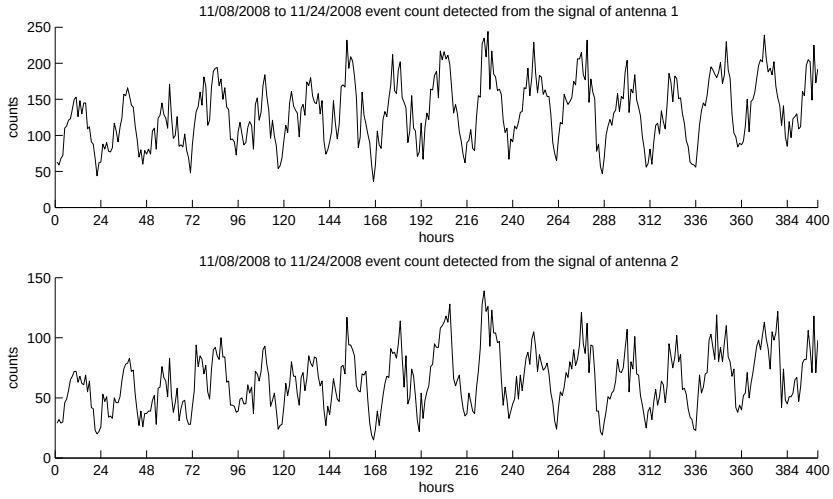

Figure 4.11: Hourly rates of candidates of meteor reflections as a function of time. The graphs span a period of 17 days [7].

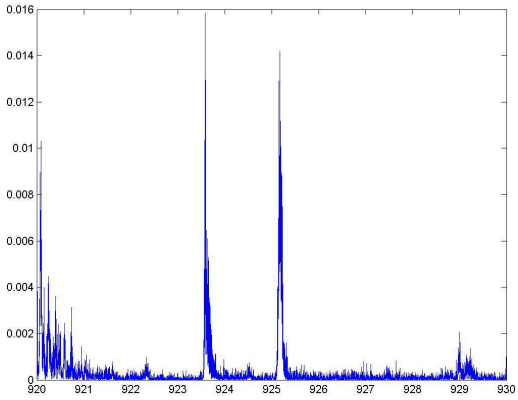

Figure 4.12: Multiple candidates (Plot duration: 10 s).

candidate. The distinct characteristic is the oscillating nature of the amplitude during the event duration accompanied by the exponential decrease.

- Dynamic noise floor: The dynamic nature of noise is shown in Figure

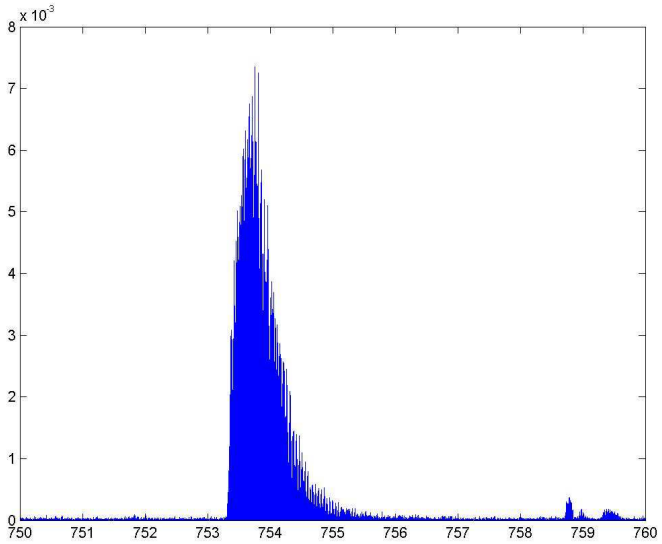

Figure 4.13: A candidate showing characteristics of underdense meteor (Plot duration: 10 s).

4.15. This kind of characteristic of noise creates a problem in the detection algorithm. Due to such erratic increases in the noise power noise sample gets classified as event. Hence complete dependence on the amplitude is strongly discouraged.

- Aircrafts: The most frequent false alarms are raised by aircrafts in the vicinity of the receiving antenna. The signals reflected by aircrafts have the typical increase in the amplitude like a signal reflected from a meteor trail. However, unlike the exponential decay of power in signals reflected by the meteor trails, the signals reflected by aircrafts have a steady increased amplitude level during the entire event duration and a sudden drop to noise floor. This feature separates short duration aircraft reflections from long duration meteors. A typical aircraft signature is shown in Figure 4.16.

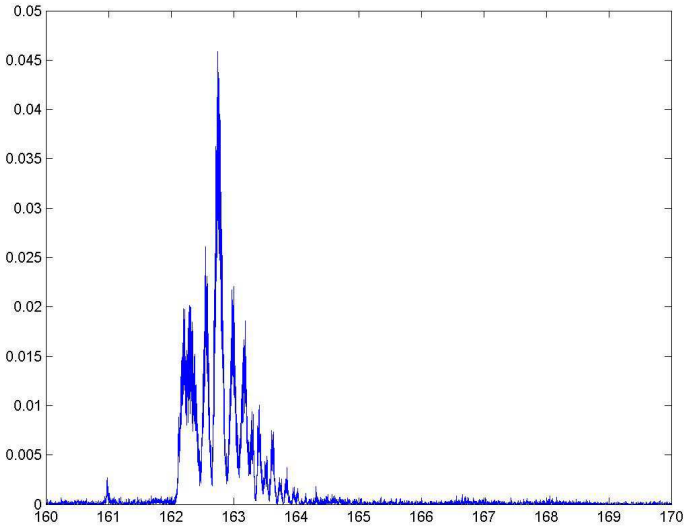

Figure 4.14: A candidate showing characteristics of possible overdense meteor (Plot duration: 10 s).

4.6 Challenges

- The phase of the local carrier heavily depends on the location of the antenna in the surrounding structures, the distance from the local transmitter and the radio noise in the surroundings. The effect can be illustrated by the analysis of three different recording stations used by MARIACHI. The best solution to this problem is selecting a site correctly.
  - Stony Brook University: This is a completely urban radio environment with lot of tall structures around the antenna, a close proximity to the local transmitter providing a continuous local reception and large number of electronic equipments operational in very close proximity. The phase of the carrier should ideally have a constant phase but in this case the histogram shows a uniform distribution. Figure 4.17 shows the distribution of the phase for 1 hour of data.
  - Custer Institute: This is a location in direct line of sight of the

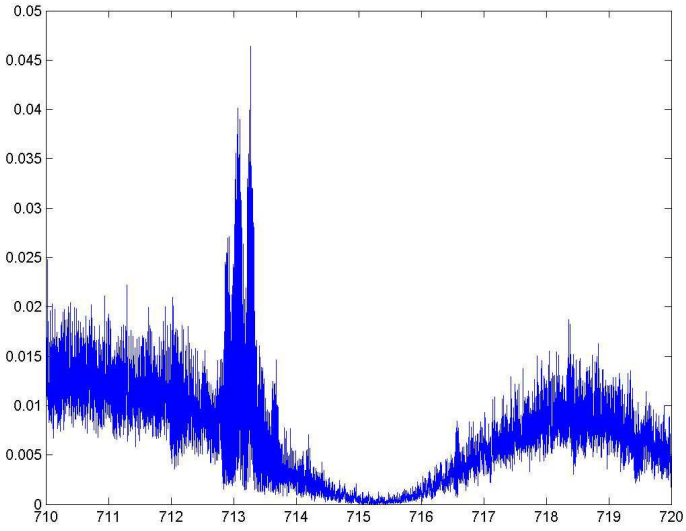

Figure 4.15: Dynamic nature of the noise floor (Plot duration: 10 s).

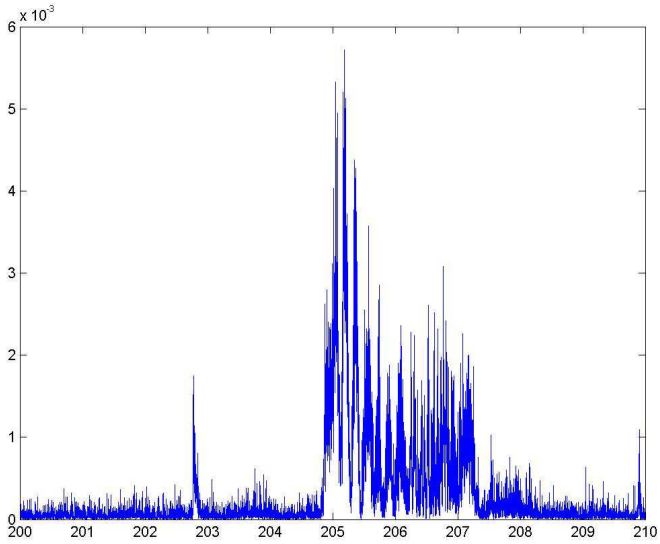

Figure 4.16: Aircraft reflection event (Plot duration: 10 s).

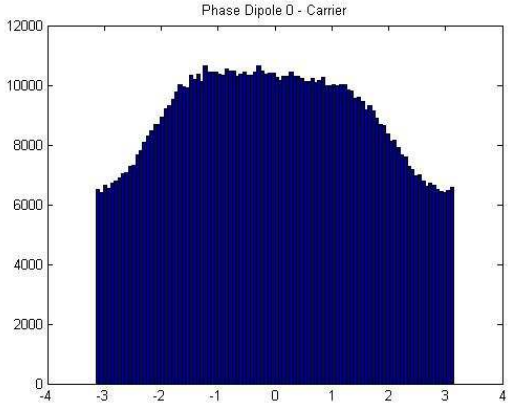

Figure 4.17: The histogram of the phase of the carrier at SBU over 1 hour.

local transmitter, and with very few local electronic interferences and open surroundings. This is a good site for setting up this kind of DAQ since the local as well as distant carriers can be recorded simultaneously. Figure 4.18 shows the distribution of the phase for 1 hour of data. The distribution does present the expected behavior with constant mean and a small deviation.

- Telescope Array, Delta, Utah: This is probably the ideal location for forward scatter radar. The location is in the middle of a valley making sure there is no direct reception of any VHF channel. Hence any signal received at the tuned frequency is definitely a reflection. This can be easily seen from the distribution of the phase shown in Figure 4.19.

- Energy threshold: Although in theory this is a good preliminary test to classify events, in practice a predefined threshold is not feasible. The average of signal energy is a dynamic quantity which depends on many factors. Hence a dynamic threshold is essential. Figure 4.20 shows the fluctuating carrier energy.

  The solution of this problem in the current algorithm is based on an hourly average energy as a reference for classification.

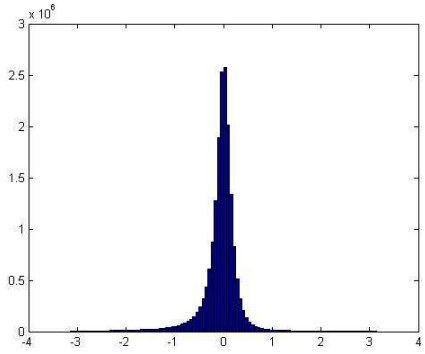

Figure 4.18: The histogram of the phase of the carrier at Custer Institute over 1 hour.

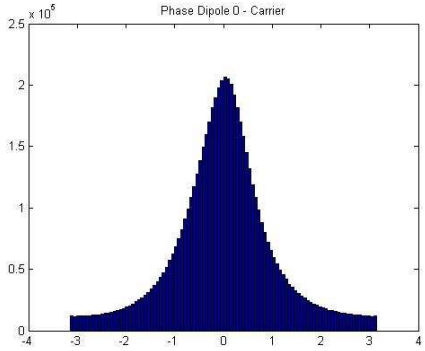

Figure 4.19: The histogram of the phase of the carrier at Telescope Array, Delta, Utah [2] over 1 hour.

- For localization, at least four synchronized stations are needed. Getting four good sites with favorable conditions has proved to be a challenge in MARIACHI.
- The data can be processed locally but even then the amount needed to be stored is very large. The source files cannot be destroyed after processing since they would be useful for future reference. Currently

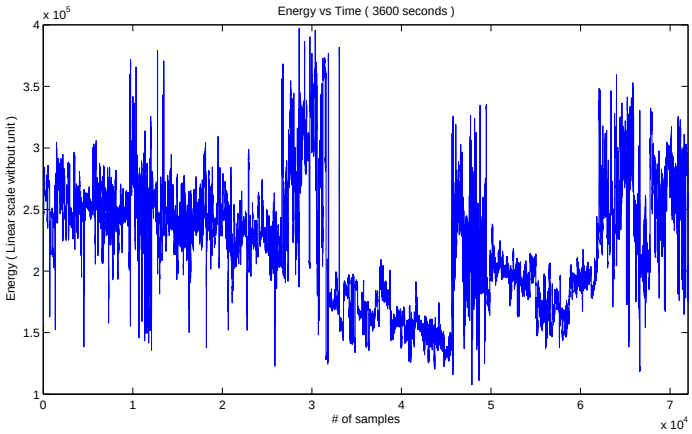

Figure 4.20: Signal energy of carrier for 1 hour data.

one hour binary file for one dipole is 2.88 GB (3600 s $\times$ 100000 samples $\times$ 8 bytes). As previously mentioned, data compression schemes are dependent on the signal processing.

- Due to the frequency drift issue, the DAQ has to lock on the local carrier as a frequency reference. The PLL technique increases the amount of spectrum to be recorded and hence the required disk space.

  Another possible solution is to provide an external stable source for local oscillator frequency, but this solution increases the cost of the DAQ. Hence a better runtime filtering algorithm is preferred in MARIACHI DAQ.

- Transition to Digital TV (DTV): Following the FCC regulation the US TV stations will start transmitting digital signals. This changes the entire spectrum of the signal. This forces us to reanalyze the setup and make necessary modifications. The idea of forward scatter will remain the same but the carrier frequencies and signal energy will change. Also the channels opting to move to UHF band will create a problem as the proposed system is meant to work strictly with VHF. The following Section will provide a brief overview of available alternatives and problems in adopting them.[2].

[2]More information regarding DTV signals can be found in [34]

4.7 Digital TV and FM radio signals

The proposed signal detection scheme is completely independent of the content of the signals, since we employ purely power-based techniques without ever demodulating the signal for information. This kind of approach gives us an opportunity to utilize differently modulated signals transmitted in the VHF region of spectrum, for meteor and cosmic ray detection. The two alternatives are DTV signals and FM radio signals.

4.7.1 DTV signals

There is a distinct dissimilarity between the analog TV signal spectrum and the DTV spectrum. The most noticeable and relevant factor is the decreased power of the carrier in the DTV signal. The spectrum of a DTV signal is as shown in Figure 4.21. In case of the DTV signal, the information coding is dictated by the 8 VSB standard [34]. Like any other digital data communication system the bits are transmitted as sinc pulses. The use of sinc pulses gives the DTV spectrum its characteristic rectangular shape.

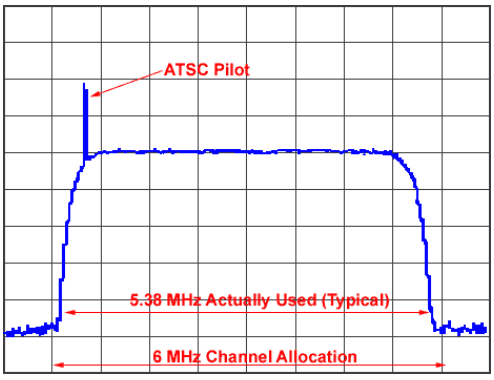

Figure 4.21: Spectrum of DTV signal

Unlike the conventional AM, where carrier is actually used to modulate the information, DTV inserts the carrier separately in the signal. This separate insertion of the carrier in the DTV signal makes the carrier independent of the data. The carrier in the case of DTV accounts only for 7% of the total signal energy in contrast to 25% in the case of analog

TV. The carrier power is generally 9-12 dB higher than the remaining DTV signal. Although the carrier is inserted at a different frequency offset within the signal, it still serves the purpose as far as the meteor or cosmic ray detection is concerned.

But the biggest concern regarding the DTV signals is their reduced transmission power. According to equation 1.1 the received power is directly proportional to the transmitted power and inversely proportional to the square of the distance between the transmitter and the receiver. Consider the calculations performed with the following parameters:

f	= 67.25 MHz
h	= 80000 m
d	= 750000 m (Considering Chapel Hill (NC) as transmitter.)
P_T	= 100 kW
G_T	= 2.5 (4 dB)
G_R	= 1
q	$= 1 \times 10^{15}\ e/m$
D	$= 10^{(0.067*(127-17*log_{10}(f)))-5.6}\ m^2/s$
λ	$= \frac{3\times10^8}{f}$ m
r_e	$= 2.818 \times 10^{-15}\ m$
R_T, R_R	$= \sqrt{d^2+h^2}$
r_0	= 0.25 m
α	$= \frac{\pi}{6}$
ϕ	$= \arcsin(\frac{h}{R_T})$
β	$= 0^\circ$

With the above parameters the received power can be computed as -84 dBm. The DTV signal is transmitted at much lower power. Assuming that all the parameters are the same, changing the transmitted power results in a received signal of -96 dBm which is well below the noise level at urban location like Stony Brook. These calculations are done under the most optimistic assumptions (without taking into account different path losses). One might argue that reducing the distance between transmitter and receiver can solve this issue. One current advantage of using DTV signals is that currently the TV spectrum of interest is sparsely occupied.

Since the detection process is independent of the modulation scheme used by the transmitter, the current setup of GNU Radio setup proves to be sufficient to carry on the DTV signal data acquisition, provided, the signal satisfies all other criteria. Due to the internal amplification provided by GNU

Radio the weak signals can also be received. However, anything below the local noise floor cannot be recovered during signal processing.

4.7.2 FM signals

Another alternative signal for this work are the FM signals, since they operate very close to the desired frequency (88-108 MHz). However, the constantly varying nature of the spectra and the low area of coverage make these signals undesirable for the proposed work. The spectrum of a FM radio station is as shown in figure 4.22. The allocated bandwidth for FM signal is 150 kHz.

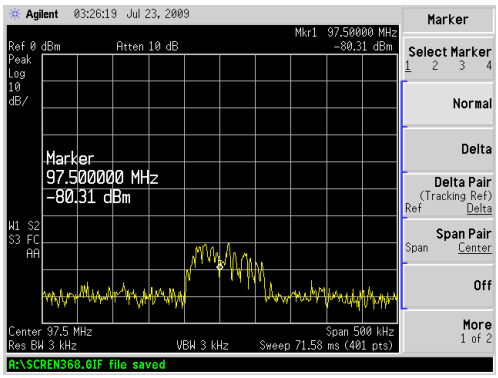

Figure 4.22: Spectrum of FM signal

The instantaneous power of the FM signal is almost completely defined by the content being transmitted at that instant. Also the FM signal does not possess any constant carrier signal as such to lock on to while recording data. Another very significant disadvantage of FM signals is the very small coverage area. The FM signals are meant to cover regions within range 100-120 km. This is partly due to the signal degradation and frequency re-usability point of view. Within a small range, the same frequency can be allocated around the country for multiple regions without any channel interference.

Chapter 5

Conclusions and future work

Cosmic ray detection has been an open problem for over a century now. During this period many different techniques have tried to exploit the characteristics of cosmic rays for their detection. The direction of arrival gives the scientists an opportunity to concentrate on a small area of the sky to look for some answers. The evolution of the field is well documented and there are ongoing efforts to improve the process.

In this thesis, we tried to present a new method for detecting cosmic rays. The idea of detecting ionized trails has been studied and used for decades now. However, we intend to extend the theory of meteor detection using radar to detect the cosmic rays. The advantages of such a data acquisition system are presented in Chapter 2.

The tools proposed for data acquisition and signal processing are based on software-defined radio. The overview of three different models used in the MARIACHI experiment are mentioned in Chapter 2 and the detailed operational description of the open source GNU Radio is provided in Chapter 3. The advantages and challenges involved in the implementation of the GNU Radio-based system are also presented in Chapter 3.

The most challenging part of the DAQ is the signal processing. The main obstacle in signal processing is the unavailability of a reference data set from any previous experiments. Hence instead of simulating synthetic data, meteors were chosen as test samples as they are the closest natural simulations of cosmic rays. The concept of detection and localization are presented in Chapter 4 along with the practical challenges involved in the entire process. The algorithms are tested with data from different locations to decrease the rate of false alarms. But it is very difficult to be absolutely

certain about the results as mentioned in Chapter 4.

The currently operational DAQ does provide a blue print for future. The process of proving the concept does provide an insight to many underlying problems which can be treated as independent research problems, such as:

- Synchronization: Probably the most critical task in setting a DAQ grid of this kind. With signals travelling at the speed of light, the room for error is minimal.
- Localization: This is the main objective of the entire experiment. The understanding of signals is needed while choosing a location to setup a recording station.
- Radios: The software-defined radio has been the back bone of the entire setup. Understanding its processing is essential to start analyzing the acquired data.
- Signal processing: The detection of reflected signals and forward scatter radar are already being studied as independent topics. However, applying them in practice to different urban and radio isolated environments needs more analysis and understanding. Also a formal statistical analysis of the data is needed.
- Data acquisition: The amount of data storage will always be a problem when such DAQs are to be setup in remote places. The problem can be solved by using an efficient data compression technique.
- Data processing: The efficiency of this module is pivotal in making the entire system cost efficient compared to all the methods of detection mentioned in Chapter 1. The software domain operation makes the system portable and a prime candidate for optimization. The parallel processing, automation and optimization can convert the system into a real time processing system.
- Digital TV (DTV): With the transition to DTV the entire spectral processing has to be revisited and modified.
- Antenna design: The current cross dipole is omni directional, but in future a more directional antenna should be designed to reduce the number of possible directions while localizing.

The results presented in this work provide the proof of concept and also highlight the need for a more sophisticated approach to implement a system for cosmic ray detection.

Bibliography

[1] *Auger Experiment website*, http://www.augere.org.

[2] *Telescope Array at Utah website*, http://www.icrr.u-tokyo.ac.jp/ ta.

[3] *Cherenkov light online reference*, http://www.mpi-hd.mpg.de/hfm/CosmicRay/ChLight/Cherenkov.html.

[4] D.W.R. McKinley, *Meteor science and engineering*, McGraw-Hill Book company Inc., 1961.

[5] Z. Zhang, "MARIACHI report on the detection of meteors by forward radio scattering," 2008.

[6] D.O. Damazio and H.Takai, "A radio detector system for ultra high energy cosmic showers," *Nuclear Science Symposium Conference Record*, vol. 1, pp. 134–138, 2003.

[7] S. Chiwate, Z. Zhang, K. Mernick, B. Shen, D. Vavilov, M.F. Bugallo, P.M. Djurić, H. Takai, and M. Marx, "SDR Based Radar System for Meteor Detection," *16th International Conference on Digital Signal Processing*, pp. 1–6, 2009.

[8] D.G. Fink, *Television Engineering*, 2nd edition, 1952.

[9] *Mixed Apparatus for Radar Investigation of Atmospheric Cosmic-rays of High Ionization, MARIACHI experiment*, http://www-mariachi.physics.sunysb.edu.

[10] F.K. Jondral, "Software-Defined Radio: Basics and Evolution to Cognitive Radio," *EURASIP Journal on Wireless Communications and Networking*, pp. 275–283, 2005.

[11] *PCR1500 website*, http://www.icomamerica.com/.

[12] *Winradio website*, http://www.winradio.com/.

[13] *AD9862 mixed-signal front-end processor for broadband communication datasheet*, http://www.analog.com/.

[14] D. Shen, *SDR Documentation*, JNL Research Group, University of Notre Dame, 2004.

[15] J.A. Goodman and R.W. Ellsworth, "Cosmic rays: Extensive air showers," *Encyclopedia of Astronomy and Astrophysics*, July 2001.

[16] J.W. Elbert and P. Sommers, "In search of a source for the 320 EeV Fly's Eye cosmic ray," *Astrophysical Journal*, vol. 441, no. 1, pp. 151–161, 1995.

[17] *Large Hadron Collider website*, http://lhc.web.cern.ch/lhc/.

[18] G.R. Sugar, "Radio propagation by reflection of meteor trails," *Proceedings of IEEE*, vol. 52, no. 2, pp. 116–136, 1964.

[19] *Federal Communication Commission*, http://www.fcc.gov.

[20] *Microtune TUNER 4937 DI5 3x7901 datasheet*, http://www.microtune.com/.

[21] *Wineguard AP 3700 VHF one pre-amplifier*, http://www.winegarddirect.com/.

[22] K. Mernick, *GNURadio MARIACHI Signal Processing*, 2008, Project report.

[23] M.P. Donadio, "CIC Filter Introduction," July 2000, http://users.snip.net/ donadio/cic.pdf.

[24] R. Andraka, "A survey of CORDIC algorithms for FPGA based computers," *Proceedings of the 1998 ACM/SIGDA Sixth International Symposium on Field Programmable Gate Arrays*, pp. 191–200, 1998.

[25] P. Beckmann, *The Depolarization of Electromagnetic Waves*, 1968, Golem Press.

[26] P.H. Young, *Electronic Communication Techniques*, 1994, Prentice Hall.

[27] A. Manikas and J.W.P Ng, "Crossed-dipole arrays asynchronous DS-CDMA systems," *IEEE transactions on Antennas and Propagation*, vol. 52, no. 1, pp. 122–131, 2004.

[28] A. Roueff, J. Chanussot, and J.I. Mars, "Estimation of polarization parameters using time-frequency representations and its application to waves separation," *Signal Process.*, vol. 86, no. 12, pp. 3714–3731, 2006.

[29] R.O. Duda, P.E. Hart, and D.G. Stork, *Pattern Classification*, 2000, Wiley-Interscience.

[30] *Spectrum Instruments, Intelligent Time reference TM4*, http://www.spectruminstruments.net/products/tm4/tm4.html.

[31] F. Zaho and L. Guibas, Morgan Kaufmann, 2004, Wireless Sensor Networks.

[32] J. Li and R.T. Compton, "Angle and polarization estimation in a coherent signal environment," *IEEE Transactions on Aerospace and Electronic Systems*, vol. 29, no. 3, pp. 706–716, July 1993.

[33] S.M. Kay, *Fundamentals of Statistical Signal Processing: Estimation Theory*, 1993, Prentice Hall.

[34] J.C. Whitaker, *DTV Handbook: The revolution in digital video*, 2001.